





MASTER THESIS 2020

# Power Electronics in DC Microgrid - Stability and Modelling

Biniam Brhane Abraham  
Rishy Kumar Saikia



**CHALMERS**  
UNIVERSITY OF TECHNOLOGY

Department of Electrical Engineering  
*Division of Electric Power Engineering*  
CHALMERS UNIVERSITY OF TECHNOLOGY  
Gothenburg, Sweden 2020

## Power Electronics In DC Micorgrid - Stability and Modelling

Biniam Brhane Abraham  
Rishy Kumar Saikia

© Biniam Brhane Abraham, Rishy Kumar Saikia 2020.

### Supervisors:

Mebtu Bihonegn Beza, Electric Power Engineering, Chalmers University of Technology  
Mattias Persson, RI.SE Research Institutes of Sweden

Examiner: Massimo Bongiorno, Electric Power Engineering, Chalmers University of Technology

Master Thesis 2020  
Department of Electrical Engineering  
Division of Electric Power Engineering  
Chalmers University of Technology  
SE-412 96, Gothenburg  
Telephone +46 31 772 1000

Typeset in L<sup>A</sup>T<sub>E</sub>X  
Printed by Chalmers Reproservice  
Gothenburg, Sweden 2020

Power Electronics in DC microgrid - Stability and Modelling  
Biniam Brhane Abraham, Rishy Kumar Saikia  
Department of Electrical Engineering  
Division of Electric Power Engineering  
Chalmers University of Technology

## Abstract

With the increasing penetration of renewables in the grid, different ways of integrating them are being researched for efficient and stable system operation. The dc-microgrid is one such system in which Distributed Energy Resources (DER) of dc nature can be parallelly connected to a common dc-bus. However, since many power converters are involved in such a system some of which act as Constant Power Load (CPL) with negative incremental resistance, this can result in system instability. Thus, the main purpose of this study is to investigate stability issue in a converter dominated dc-microgrid.

In this thesis, the Topology and operational principle of boost converter, bi-directional DC/DC converter and two-level Voltage Source Converter (VSC) is first studied and their input impedance models are derived. Moreover, simulation models of the converters are created and the analytical transfer functions are verified with the simulation models by frequency-domain approach. Finally, the stability of the total system derived analytically is studied using stability analysis methods such as Nyquist criteria and passivity analysis.

Findings show that, when the load in the dc system is increased by 40% from 50 kW to 70 kW, the system stability decreases due to worsening of passivity of the CPL. In addition to this, when the voltage and current controller bandwidths of the VSC is increased it is found that the voltage controller parameter has more effect on the system stability than the current controller. Moreover, addition of a battery storage system to the dc grid shows that it integrates well during the charging process, but with a reduced stability margin. During the discharging of the energy storage, the system works in an islanded mode and remains stable for a short duration depending on the energy storage capacity. Furthermore, a capacitor bank consisting of eight capacitors with 7 mF capacitance each is connected to the system in series and parallel configuration and it is observed that the system is more stable, however, the response becomes slower. Finally, it is also investigated that the droop controller of the VSC has little effect on the system stability.

**Keywords:** DC microgrid, stability analysis, DER - Distributed Energy Resources, PV - Photovoltaic, Nyquist criteria, Passivity analysis, VSC - Voltage Source Converter, controller bandwidth, battery storage, islanded mode, capacitor bank, droop controller.

## Acknowledgements

We would express our sincere gratitude to our supervisors, Mebtu Bihonegn Beza (Division of Electric Power Engineering) and Mattias Persson (RI.SE Research Institutes of Sweden) for their support, guidance and encouragement throughout the thesis work. They have always been available to answer our questions and queries and also provide us with valuable feedback for our work. We also want to thank our examiner, Massimo Bongiorno (Division of Electric Power Engineering) for his support, advice and allowing us the freedom to explore and implement our ideas.

We are thankful to everyone in the Division of Electric Power Engineering for providing us with useful resources and also to RI.SE for giving us the opportunity to visit the dc system and understand it better.

Finally, we would like to thank our family and friends for all support and encouragement throughout the project and also our study in Chalmers.

Biniam Brhane Abraham and Rishy Kumar Saikia, Gothenburg, October 2020

# Contents

<b>List of Figures</b>	<b>viii</b>
<b>List of Tables</b>	<b>x</b>
<b>1 Introduction</b>	<b>2</b>
1.1 Introduction . . . . .	2
1.2 Purpose of Work . . . . .	3
1.3 Outline of the Thesis . . . . .	3
<b>2 Theory</b>	<b>5</b>
2.1 System Overview . . . . .	5
2.2 Stability Issues in DC-Microgrids . . . . .	5
2.3 PV Energy Source . . . . .	6
2.3.1 Boost Converter Model . . . . .	6
2.3.2 MPPT Control Algorithm . . . . .	10
2.4 Energy Storage System . . . . .	11
2.4.1 Bidirectional DC/DC Converter Model Working in Discharging Mode . . . . .	12
2.4.2 Bidirectional DC/DC Converter Model Working in Charging Mode . . . . .	16
2.5 Modelling of Loads . . . . .	18
2.5.1 Resistive Loads . . . . .	18
2.5.2 Constant Power Load (CPL) Model . . . . .	18
2.6 Grid Source Interface . . . . .	19
2.6.1 Voltage Source Converter Model . . . . .	19
2.6.2 Control Parameter Selection . . . . .	23
2.7 Stability Analysing Techniques . . . . .	24
2.7.1 Eigenvalue Analysis . . . . .	24
2.7.2 Nyquist Stability Criterion . . . . .	24
2.7.3 Passivity Analysis of the System . . . . .	24
<b>3 System Modelling</b>	<b>27</b>
3.1 Modelling of DC-microgrid Analytically . . . . .	27
3.1.1 Impedance Model on PV side Converter . . . . .	27
3.1.2 Admittance Model of CPL . . . . .	28
3.1.3 Admittance Model of Energy Storage Converter . . . . .	29
3.1.4 Impedance Model of Voltage Source Converter . . . . .	29
3.2 Modelling of DC-microgrid in Simulink . . . . .	29

3.2.1	PV Model . . . . .	29
3.2.2	Energy Storage Model . . . . .	30
3.2.3	VSC Model . . . . .	31
3.2.4	CPL Model . . . . .	32
3.3	Verification of Impedance Models . . . . .	32
3.3.1	Verification of VSC Impedance Model . . . . .	33
3.3.2	Verification of PV Impedance Model . . . . .	34
3.3.3	Verification of Energy Storage Impedance Model . . . . .	36
3.3.3.1	Bidirectional Converter Working as Boost Converter	36
3.3.3.2	Bidirectional Converter Working as Buck Converter .	37
3.4	Passivity Analysis of Individual Systems . . . . .	38
3.5	Simplified Model of the System . . . . .	40
<b>4</b>	<b>Results and Analysis</b>	<b>43</b>
4.1	Case Scenario One: Normal Working Condition . . . . .	43
4.2	Case Scenario Two: Effect of Increasing Load . . . . .	46
4.3	Case Scenario Three: Effect of Increasing Controller Bandwidth . . . . .	47
4.3.1	Increasing VSC Voltage Controller Bandwidth . . . . .	48
4.3.2	Increasing VSC Current Controller Bandwidth . . . . .	50
4.4	Case Scenario Four: Effect of Adding Energy Storage . . . . .	51
4.4.1	Charging Mode . . . . .	52
4.4.2	Discharging (Islanded) Mode . . . . .	54
4.5	Case Scenario Five: Effect of Adding a Capacitor Bank . . . . .	56
4.6	Case Scenario Six: Effect of Adding a Droop Control . . . . .	58
<b>5</b>	<b>Sustainability</b>	<b>61</b>
5.1	Sustainability Aspects . . . . .	61
5.1.1	Ecological Aspect . . . . .	61
5.1.2	Economical Aspect . . . . .	61
5.1.3	Social aspect . . . . .	61
<b>6</b>	<b>Conclusion and Future Work</b>	<b>63</b>
6.1	Conclusion . . . . .	63
6.2	Future Work . . . . .	64
	<b>Bibliography</b>	<b>65</b>
	<b>Bibliography</b>	<b>65</b>
<b>A</b>	<b>Appendix 1</b>	<b>I</b>
A.1	Capacitance Calculation of Capacitor Bank . . . . .	I

# List of Figures

2.1	Topology of a boost converter with a duty cycle controller. . . . .	7
2.2	Topology of a bi-directional converter with discharging mode control. . . . .	12
2.3	Small signal control diagram with droop controller. . . . .	15
2.4	Topology of a bi-directional converter with charging mode control. . . . .	16
2.5	Small signal control diagram (charging). . . . .	17
2.6	Voltage v/s Current characteristic for a CPL. . . . .	18
2.7	A CPL consisting of a tightly regulated converter and a resistive load. . . . .	19
2.8	Model of the AC grid and VSC. . . . .	20
2.9	Control diagram of a VSC. . . . .	20
2.10	Small-signal model for control of VSC. . . . .	24
3.1	PI model of cables between the PV converter and DC-bus line. . . . .	28
3.2	PV model for panels located at AWL and SB3. . . . .	29
3.3	PV model AWL building. . . . .	30
3.4	Simulation model for the energy storage system. . . . .	30
3.5	Energy storage control model (charging and discharging). . . . .	31
3.6	Simulation model of the VSC. . . . .	31
3.7	Simulation model of the CPL consisting of a tightly regulated converter and a resistive load. . . . .	32
3.8	Impedance verification of VSC for analytical and simulation models for various frequencies. . . . .	33
3.9	PV array module from Simulink used for specifying reference voltage[1]. . . . .	34
3.10	I-V and P-V characteristics of the PV array type: SunPower SPR-315E-WHT-D; 7 series modules; 3 parallel strings at 25°and 45°[1]. . . . .	35
3.11	Impedance verification of PV system for analytical and simulation models. . . . .	36
3.12	Impedance verification of energy storage discharging. . . . .	37
3.13	Impedance verification of energy storage - charging. . . . .	38
3.14	Passivity plots for PV impedance model. . . . .	38
3.15	Passivity plots for energy storage impedance for charging. . . . .	39
3.16	Passivity plots for VSC output impedance. . . . .	39
3.17	An equivalent model of the dc-microgrid for impedance based analysis. . . . .	41
3.18	A simplified circuit of the dc-grid. . . . .	41
3.19	Circuit connection of the capacitor bank. . . . .	42
4.1	Nyquist and Pole-Zero plots of the open loop transfer function $F(s)$ for normal working condition. . . . .	44

4.2	Gain and phase margins of open loop transfer function $F(s)$ for the normal operating condition. . . . .	44
4.3	PV output plots for the grid connected system. . . . .	45
4.4	Grid connected VSC output plots. . . . .	46
4.5	Bode plot comparison for increasing load from 50 kW to 70 kW. . . .	46
4.6	DC bus voltage for a 20 kW load step from 50 kW to 70 kW at 0.2 s. .	47
4.7	Nyquist and Pole-Zero map of open loop transfer function $F(s)$ for increasing VSC voltage controller bandwidths of 10 Hz, 20 Hz and 30 Hz. 48	
4.8	Bode plots of open loop transfer function $F(s)$ for increasing voltage controller bandwidths of 10 Hz, 20 Hz and 30 Hz. . . . .	48
4.9	Frequency response of VSC for increasing voltage controller bandwidth from 10 Hz, 20 Hz to 20 Hz. . . . .	49
4.10	Nyquist and Pole-Zero map of open loop transfer function $F(s)$ for increasing VSC current controller bandwidths of 100 Hz, 200 Hz and 300 Hz. . . . .	50
4.11	Bode plots of open loop transfer function $F(s)$ for increasing VSC current controller bandwidth of 100 Hz, 200 Hz and 300 Hz. . . . .	50
4.12	Frequency response of VSC for increasing current controller bandwidths. 51	
4.13	Nyquist and Pole-Zero map of open loop transfer function $F(s)$ with and without energy storage during charging. . . . .	52
4.14	Bode plot of open loop transfer function $F(s)$ for energy storage model in charging mode. . . . .	52
4.15	DC bus voltage during charging mode with an energy storage added at 0.2 s. . . . .	53
4.16	Charging wave forms for the energy storage. . . . .	54
4.17	Bode plot for the the energy storage model during discharge. . . . .	55
4.18	Discharge waveform for the energy storage. . . . .	55
4.19	Nyquist and Pole-zero map of open loop transfer function $F(s)$ with and without a capacitor bank. . . . .	56
4.20	Frequency response of the VSC after adding a capacitor bank. . . . .	57
4.21	Bode plot of open loop transfer function $F(s)$ with a capacitor bank added to the system. . . . .	57
4.22	DC-bus voltage with and without a capacitor bank for a load step of 20 kW at 0.7 s. . . . .	58
4.23	Nyquist and Pole-Zero map of open loop transfer function $F(s)$ for for increasing droop. . . . .	59
4.24	Bode plots for increasing droop of VSC starting with no droop, 5% droop and 10% droop. . . . .	59
4.25	Frequency response of VSC for increasing droop gain. . . . .	60
A.1	Capacitor bank schematic of the real system. . . . .	I

# List of Tables

3.1	Cable parameters [2], [3]. . . . .	28
3.2	Rated values of VSC. . . . .	33
3.3	Rated values of PV converter. . . . .	35
3.4	Rated values of energy storage (discharging). . . . .	36
3.5	Rated values of energy storage (charging). . . . .	37

## List of abbreviations

<b>DC</b>	Direct Current
<b>AC</b>	Alternating Current
<b>CPL</b>	Constant Power Load
<b>PV</b>	Photo Voltaic
<b>DER</b>	Distributed Energy Resources
<b>CCL</b>	Constant Current Load
<b>CRL</b>	Constant Resistive Load
<b>MPPT</b>	Maximum Power Point Tracking
<b>PWM</b>	Pulse Width Modulator
<b>POL</b>	Point of Load
<b>VSC</b>	Voltage Source Converter
<b>PCC</b>	Point of Common Coupling
<b>PLL</b>	Phase Locked Loop
<b>PI</b>	Proportional Integral Controller
<b>SSO</b>	Solar String Optimizers
<b>FFT</b>	Fast Fourier Transform
<b>DCR</b>	Direct Current Resistance
<b>DPS</b>	Distributed Power System
<b>SOC</b>	State of Charge
<b>MGF</b>	Mason's Gain Formula
<b>BESS</b>	Battery Energy Storage System

# 1

## Introduction

### 1.1 Introduction

With a growing human population and improving living standards, the demand for energy has increased. Although fossil fuels have been fulfilling our energy demand for a long time, emissions from fossil-based power sources have adversely affected our environment, resulting in an increased global temperature and climate change. It is in this context that focus has shifted on harnessing renewable energy sources. With the increasing penetration of renewables into the modern electric grid, the concept of microgrid was proposed several years ago due to many of its advantages like energy efficiency and environmental benefits [4]. These microgrids can be classified into Alternate Current (AC) and Direct Current (DC) type. ac-microgrids have an advantage of utilizing existing ac power grid infrastructure but they require complicated control strategies for the synchronization process and maintaining system stability [5],[6]. DC microgrids, unlike ac ones, have a better approach in integrating renewable energy sources with a dc-link as distributed energy sources are inherently dc.

Renewable energy sources and storage devices are interfaced to the dc-grid via high efficiency tightly regulated power converters. These converters act as a CPL with a negative incremental resistance that reduces the system stability margin since the overall system is poorly damped [7]. Furthermore, the dynamics of the ac control loop together with the pulse-width modulator (PWM) in a VSC could cause instability. Besides, to increase the scalability of the system several modules are used in parallel and this could lead to instability due to low inertia in the integrated power converters [8].

## 1.2 Purpose of Work

In this project, a realistic dc-microgrid consisting of Photo Voltaic (PV) energy source, a Battery Energy Storage System (BESS), dc-loads connected to it and the overall dc system connected to the main ac grid will be studied. It is a converter dominated system and the study will focus on the stability issues and modelling of the converters to observe the impact of operating closer to instability.

A proposed method to detect such issues is by applying small-signal stability analysis and then develop suitable models to study the stability issues in such dc systems. For stability assessment, frequency domain analysis will be performed as it is useful in understanding stability contribution from individual converters in the system [9]. The converters, both DC/DC and AC/DC will be modelled based on their transfer functions without going into internal dynamics. Furthermore, for the AC/DC converter, only dc side stability which is interfaced with the dc-microgrid will be studied.

The study will be carried out in the ac grid-connected mode so that the dc-bus voltage is regulated by the ac source. Batteries are taken as energy storage units without going into their internal working. Moreover, for stability study, only short duration disturbance is considered.

## 1.3 Outline of the Thesis

In this study, Chapter 2 describes the theory related to the overall dc-microgrid. This includes the derivation of impedance models for each of the converters used in the system and also discusses the stability analysis methods. Chapter 3 describes the methodology of how impedance and admittance models are derived from the relationships derived in Chapter 2. It also includes a verification of derived impedance transfer functions with simulation models designed with the same parameters. Chapter 4 discusses the case scenarios and the results obtained. Chapter 5 discusses the sustainable aspect of the study. Finally, Chapter 6 concludes the study with suggestions and ideas for improvement in future work.



# 2

## Theory

This chapter explains the overall dc-microgrid system. Section 2.1-2.2, describes the system in general, regarding how it works overall and the potential sources of instability for the system. In Section 2.3, PV source is explained including the converter and its control strategy. In Section 2.4, the BESS consisting of battery banks is described, with the converter in its two working modes, charging and discharging. Section 2.5 describes the CPL model for the study. In Section 2.6, the ac grid-side interface is described with its converter topology and control structure.

### 2.1 System Overview

In the dc-microgrid system, PV panel arrays provide power for the loads and also to charge the BESS. Power from the PV arrays is extracted using maximum power point tracking (MPPT), so that it is transferred with the highest efficiency even with varying irradiance levels. From the PV side, input power is controlled considering a maximum power operating point and it is fed to a boost DC/DC converter. Therefore, the duty cycle of the converter is regulated based on the reference voltage required for the maximum power. The output of the boost converter is not strictly maintained at the bus voltage but within a desirable range. The dc-bus voltage is maintained at a fixed value by the voltage source AC/DC converter. It also either feeds power from the grid to the dc-bus line when PV is unable to provide the power demand or feeds back to the grid when excess power is generated by the PV. In the BESS, a bi-directional buck-boost converter is used to charge-discharge from the battery pack. During normal operation, when PV is supplying power, the batteries are charged and also gives power to the load. But when load demand is more than the power PV supplies, the VSC provides the additional power required. As in [10], the loads connected to the dc-bus have a relatively faster response compared to the converters and can be taken as a CPL.

### 2.2 Stability Issues in DC-Microgrids

DC-microgrid systems have many power converters and different types of dc-loads connected to it. These converters when operating independently could be stable. However, when many such converters are connected to a common output bus, there could be interaction among them which could lead to instability of the overall system. Moreover, CPLs in the system have a negative resistance characteristic which can

reduce the overall system stability. In this thesis, the resultant interaction of the power converters and CPLs is the main focus of study.

## 2.3 PV Energy Source

Photovoltaic cells capture photons from sunlight and generate electrons, an array of such cells combined together can be used to obtain a desired power and voltage level. The output voltage from such arrays of PV panel is low and as such a boost converter is needed to step up the voltage. Since power only flows from the panel to the dc-microgrid side, it is modeled as unidirectional. Moreover, the output power from the solar panel keeps varying due to environmental conditions. This requires for most efficient extraction of power at any point. For this purpose, as in [11], an MPPT is used, which continuously tracks the power from the PV panel and adjusts the voltage accordingly to obtain maximum power.

### 2.3.1 Boost Converter Model

A boost converter is a DC/DC converter that steps up a voltage and is used in a low output voltage and unidirectional energy source. It consists of a switch (MOSFET) that turns on-off periodically depending on an input duty cycle. The steady-state duty cycle,  $D$  is calculated from the reference voltage,  $V_{ref}$  and steady-state output voltage,  $V_{dc}$  ( $D = 1 - \frac{V_{ref}}{V_{dc}}$ ). To track the maximum power production, the duty cycle has to be adjusted. Thus, to regulate the duty cycle, the PV voltage output from the converter is compared with a desired PV reference output voltage (taken from the maximum power operating point). This difference is fed to a proportional (P) controller, which then generates a controlled signal to a pulse width modulator (PWM), thereby generating the switching signals [11]. This converter topology suits in PV systems with a low output voltage. The converter circuit is shown as in Figure 2.1 along with its control structure and its mathematical model has also been derived.

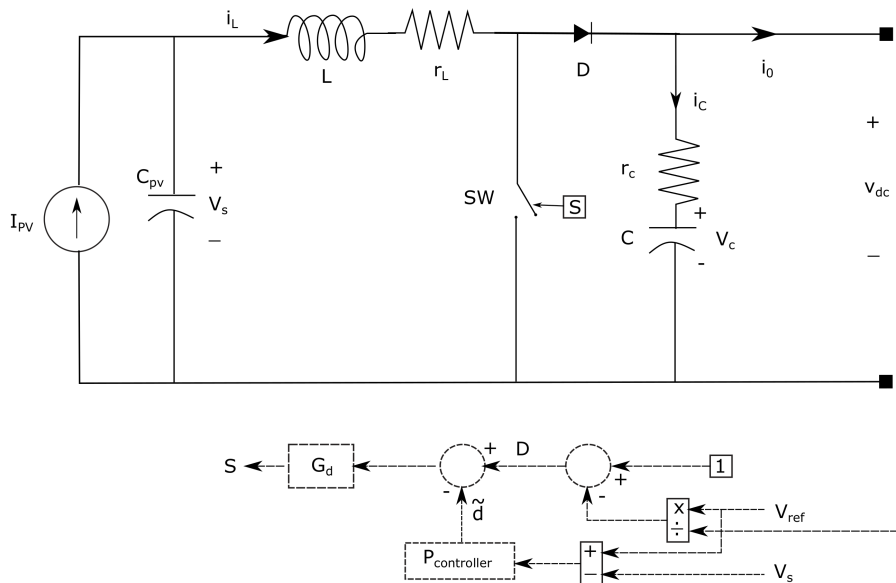


**Figure 2.1:** Topology of a boost converter with a duty cycle controller.

Figure 2.1 is the circuit diagram for the PV boost converter. On the source side, the PV panel is a current source in parallel with a capacitor,  $C_{pv}$ , which serves as the source voltage,  $v_s$ . In this converter, the focus is on obtaining maximum power from the source without directly regulating the PV output voltage,  $v_{dc}$ . For achieving this, a voltage reference,  $V_{ref}$  is used for a particular power level from the PV which is dependent on a specific irradiance at a particular temperature. This reference voltage is divided by the output voltage of the boost converter and then subtracted from one to generate a steady-state duty cycle. Furthermore, the reference voltage is compared with the source voltage and passed through a proportional (P) controller to generate a varying duty cycle. This would accordingly increment or decrement the steady-state duty cycle and adjust it depending on the input power from the panels. Thus, by this control technique, the input voltage,  $v_s$ , is controlled to get the maximum power from PV [11].

Now, state space averaging is used to derive the converter model. There are two topologies which are applied during the switch on and switch off of the converter.

When the switch is closed

$$\frac{di_L}{dt} = \frac{v_s}{L} - \frac{r_L i_L}{L} \quad (2.1)$$

$$\frac{dv_c}{dt} = \frac{-i_o}{C} \quad (2.2)$$

$$\begin{aligned} v_{dc} &= v_c + r_c i_c \\ v_{dc} &= v_c - r_c i_o \end{aligned} \quad (2.3)$$

where  $v_s$  and  $v_{dc}$  are the PV side voltage and dc-link voltage respectively,  $L$  and  $C$  are the inductor and capacitor components of the converter,  $v_c$  is the voltage across the capacitor,  $i_o$  is the output current and is negative of the capacitor current,  $i_c$ , during the switch-on time and  $r_c$  is the equivalent series resistance of the capacitor.

Equations 2.1, 2.2 and 2.3 can be written in state-space representation as

$$\begin{bmatrix} \frac{di_L}{dt} \\ \frac{dv_c}{dt} \end{bmatrix} = \begin{bmatrix} -\frac{r_L}{L} & 0 \\ 0 & 0 \end{bmatrix} \begin{bmatrix} i_L \\ v_c \end{bmatrix} + \begin{bmatrix} 0 \\ \frac{-1}{C} \end{bmatrix} i_o + \begin{bmatrix} \frac{1}{L} \\ 0 \end{bmatrix} v_s \quad (2.4)$$

$$v_{dc} = \begin{bmatrix} 0 & 1 \end{bmatrix} \begin{bmatrix} i_L \\ v_c \end{bmatrix} - r_c \cdot i_o. \quad (2.5)$$

When the switch is open

$$\begin{aligned} \frac{di_L}{dt} &= -\frac{r_l}{L} - \frac{r_c i_c}{L} - \frac{v_c}{L} + \frac{v_s}{L} \\ \frac{dv_c}{dt} &= \frac{i_L}{C} - \frac{i_o}{C} \\ v_{dc} &= v_c + r_c i_c \\ i_c &= i_L - i_o. \end{aligned} \quad (2.6)$$

Replacing  $i_c$  by  $i_L - i_o$ , then the equations can be expressed as

$$\frac{di_L}{dt} = -\frac{(r_l + r_c)i_L}{L} + \frac{r_c i_o}{L} - \frac{v_c}{L} + \frac{v_s}{L} \quad (2.7)$$

$$\frac{dv_c}{dt} = \frac{i_L}{C} - \frac{i_o}{C} \quad (2.8)$$

$$v_{dc} = v_c + r_c i_L - r_c i_o. \quad (2.9)$$

Equations (2.7)-(2.9) can be written in state space form as following

$$\begin{bmatrix} \frac{di_L}{dt} \\ \frac{dv_c}{dt} \end{bmatrix} = \begin{bmatrix} \frac{-(r_l+r_c)}{L} & \frac{-1}{L} \\ \frac{1}{C} & 0 \end{bmatrix} \begin{bmatrix} i_L \\ v_c \end{bmatrix} + \begin{bmatrix} \frac{r_c}{L} \\ \frac{-1}{C} \end{bmatrix} i_o + \begin{bmatrix} \frac{1}{L} \\ 0 \end{bmatrix} v_s \quad (2.10)$$

$$v_{dc} = \begin{bmatrix} r_c & 1 \end{bmatrix} \begin{bmatrix} i_L \\ v_c \end{bmatrix} - r_c \cdot i_o. \quad (2.11)$$

The state equations derived above can be expressed as compact matrix form

$$\dot{x} = \mathbf{A}x(t) + \mathbf{B}U(t) \quad (2.12)$$

$$y = \mathbf{C}x(t) + \mathbf{E}U(t) \quad (2.13)$$

where  $x(t)$  represents the state space variables and  $U(t)$  represents input and output variables in the model. Average matrices that include the two switching events at steady state are given as

$$A = A_1 d + A_2 (1 - d) \quad (2.14)$$

$$B_1 = B_{11} d + B_{21} (1 - d) \quad (2.15)$$

$$B_2 = B_{12} d + B_{22} (1 - d) \quad (2.16)$$

$$C = C_1 d + C_2 (1 - d) \quad (2.17)$$

$$E = E_1 d + E_2(1 - d) \quad (2.18)$$

where  $d$  is the duty cycle and the  $B$  matrix has been split into two matrices, because in this model there are two variables,  $i_o$  and  $v_s$  under the  $U(t)$  variable. Combining the matrices (2.4) and (2.10)

$$A_1 = \begin{bmatrix} -\frac{r_l}{L} & 0 \\ 0 & 0 \end{bmatrix} B_{11} = \begin{bmatrix} 0 \\ \frac{-1}{C} \end{bmatrix} B_{12} = \begin{bmatrix} \frac{1}{L} \\ 0 \end{bmatrix} C_1 = \begin{bmatrix} 0 & 1 \end{bmatrix} E_1 = -r_c \quad (2.19)$$

$$A_2 = \begin{bmatrix} \frac{-(r_l+r_c)}{L} & \frac{-1}{C} \\ \frac{1}{C} & 0 \end{bmatrix} B_{21} = \begin{bmatrix} \frac{r_c}{L} \\ \frac{-1}{C} \end{bmatrix} B_{22} = \begin{bmatrix} \frac{1}{L} \\ 0 \end{bmatrix} C_2 = \begin{bmatrix} r_c & 1 \end{bmatrix} E_2 = -r_c \quad (2.20)$$

$$\begin{bmatrix} \dot{i}_L \\ \dot{v}_c \end{bmatrix} = [A_1 d + A_2(1 - d)] \begin{bmatrix} i_L \\ v_c \end{bmatrix} + [B_{11} d + B_{12}(1 - d)] i_o + [B_{21} d + B_{22}(1 - d)] v_s. \quad (2.21)$$

To analyse the small-signal model of the converter, a small ac perturbation is introduced in the steady-state quantities. Therefore, all variables mentioned above will be written as

$$i_L = I_L + \tilde{i}_L \quad (2.22)$$

$$v_c = V_c + \tilde{v}_c \quad (2.23)$$

$$v_{dc} = V_{dc} + \tilde{v}_{dc} \quad (2.24)$$

$$i_o = I_o + \tilde{i}_o \quad (2.25)$$

$$d = D + \tilde{d}. \quad (2.26)$$

Inserting (2.24) into (2.21) and arranging it to get the average matrix

$$\begin{aligned} \begin{bmatrix} \dot{\tilde{i}}_L \\ \dot{\tilde{v}}_c \end{bmatrix} &= [A_1 D + A_2(1 - D) + (A_1 - A_2)\tilde{d}] \begin{bmatrix} I_L + \tilde{i}_L \\ V_c + \tilde{v}_c \end{bmatrix} + \\ & [B_{11} D + B_{21}(1 - D) + (B_{11} - B_{21})\tilde{d}] [I_o + \tilde{i}_o] + \\ & [B_{12} D + B_{22}(1 - D) + (B_{12} - B_{22})\tilde{d}] [V_s + \tilde{v}_s] \end{aligned} \quad (2.27)$$

$$\begin{aligned} V_{dc} + \tilde{v}_{dc} &= [C_1 D + C_2(1 - D) + (C_1 - C_2)\tilde{d}] \begin{bmatrix} I_L + \tilde{i}_L \\ V_c + \tilde{v}_c \end{bmatrix} + \\ & [E_1 D + E_2(1 - D) + (E_1 - E_2)\tilde{d}] [I_o + \tilde{i}_o] \end{aligned} \quad (2.28)$$

where in steady state  $\dot{I}_L$  and  $\dot{V}_c$  are zero. The matrix is simplified by eliminating the steady state values and the product of the perturbations. Finally, the small signal model is simplified as

$$\begin{bmatrix} \dot{\tilde{i}}_L \\ \dot{\tilde{v}}_c \end{bmatrix} = A \begin{bmatrix} \tilde{i}_L \\ \tilde{v}_c \end{bmatrix} + \left[ [A_1 - A_2] \begin{bmatrix} I_L \\ V_c \end{bmatrix} + [B_{11} - B_{21}] I_o + [B_{12} - B_{22}] V_s \right] \tilde{d} + B_1 \tilde{i}_o + B_2 \tilde{v}_s \quad (2.29)$$

$$\tilde{v}_{dc} = C \begin{bmatrix} \tilde{i}_L \\ \tilde{v}_c \end{bmatrix} + \left[ [C_1 - C_2] \begin{bmatrix} I_L \\ V_c \end{bmatrix} + [E_1 - E_2] I_o \right] \tilde{d} + E \tilde{i}_o. \quad (2.30)$$

To analyse the transfer function in s-domain, Laplace transformation is applied to (2.29) and (2.30)

$$\begin{bmatrix} s\tilde{i}_L(s) \\ s\tilde{v}_c(s) \end{bmatrix} = A \begin{bmatrix} \tilde{i}_L(s) \\ \tilde{v}_c(s) \end{bmatrix} + \left[ [A_1 - A_2] \begin{bmatrix} I_L \\ V_c \end{bmatrix} + [B_{11} - B_{21}] I_o + [B_{12} - B_{22}] V_s \right] \tilde{d}(s) + B_1 \tilde{i}_o(s) + B_2 \tilde{v}_s(s) \quad (2.31)$$

$$\tilde{v}_{dc}(s) = C \begin{bmatrix} \tilde{i}_L(s) \\ \tilde{v}_c(s) \end{bmatrix} + \left[ [C_1 - C_2] \begin{bmatrix} I_L \\ V_c \end{bmatrix} + [E_1 - E_2] I_o \right] \tilde{d}(s) + E \tilde{i}_o(s) \quad (2.32)$$

$$\begin{bmatrix} \tilde{i}_L(s) \\ \tilde{v}_c(s) \end{bmatrix} = (sI - A)^{-1} \left[ \begin{bmatrix} [A_1 - A_2] \begin{bmatrix} I_L \\ V_c \end{bmatrix} + [B_{11} - B_{21}] I_o + [B_{12} - B_{22}] V_s \\ B_1 \tilde{i}_o(s) + B_2 \tilde{v}_s(s) \end{bmatrix} \tilde{d}(s) + \right] \quad (2.33)$$

equation (2.33) is substituted in (2.32) and it yields

$$\tilde{v}_{dc}(s) = \left[ \begin{array}{c} C(sI - A)^{-1} \left[ [A_1 - A_2] \begin{bmatrix} I_L \\ V_c \end{bmatrix} + [B_{11} - B_{21}] I_o + [B_{12} - B_{22}] V_s \right] + \\ [C_1 - C_2] \begin{bmatrix} I_L \\ V_c \end{bmatrix} + [E_1 - E_2] I_o \end{array} \right] \tilde{d}(s) + [C(sI - A)^{-1} B_1 + E] \tilde{i}_o(s) + C(sI - A)^{-1} B_2 \tilde{v}_s(s). \quad (2.34)$$

Equation (2.34) is the small signal dc-link voltage expression from the boost converter.

### 2.3.2 MPPT Control Algorithm

In an MPPT controller, the PV side voltage and power from the panel are continuously tracked. This is then fed to a controller which generates the duty cycle for the boost converter. It works in a way to control the PV side voltage,  $v_s$ , to the boost converter so that the maximum power is always taken from the PV panel.

From the basic boost converter operation, the duty cycle is calculated as

$$d = 1 - \frac{v_s}{v_{dc}} \quad (2.35)$$

where  $v_s$  and  $v_{dc}$  are the PV voltage and dc-link voltage. Then, the small signal analysis will be

$$D + \tilde{d} = 1 - \frac{V_{ref} + \tilde{v}_s}{V_{dc} + \tilde{v}_{dc}} \quad (2.36)$$

where,  $V_{ref}$ , is the reference output voltage for PV array at maximum output power and is equal to zero in small signal analysis. Thus, the perturbation of the duty cycle is expressed as

$$\tilde{d} = -\frac{\tilde{v}_s}{V_{dc}} + \frac{V_s}{V_{dc}^2} \tilde{v}_{dc}. \quad (2.37)$$

Moreover, PV is working as a current source and the duty cycle depends on the changing of the input voltage as in [11]

$$\tilde{d} = -P\tilde{v}_s. \quad (2.38)$$

Here,  $P$  is a proportional constant and combining (2.37) and (2.38) yields

$$P\tilde{v}_s = \frac{\tilde{v}_s}{V_{dc}} - \frac{V_s \tilde{v}_{dc}}{V_{dc}^2} \quad (2.39)$$

$$\tilde{v}_s = \frac{-V_s}{V_{dc}(PV_{dc} - 1)} \tilde{v}_{dc} \quad (2.40)$$

$$\tilde{d} = \frac{PV_s}{V_{dc}(PV_{dc} - 1)} \tilde{v}_{dc}. \quad (2.41)$$

Taking coefficients of (2.34) as X, S and R for  $\tilde{d}$ ,  $\tilde{i}_o$  and  $\tilde{v}_s$  respectively for simplifying the derivation. Then, inserting (2.40) and (2.41) into (2.34) and it is expressed as

$$\tilde{v}_{dc} = \frac{XPV_s}{V_{dc}(PV_{dc} - 1)} \tilde{v}_{dc} + S\tilde{i}_o + \frac{-RV_s}{V_{dc}(PV_{dc} - 1)} \tilde{v}_{dc}. \quad (2.42)$$

Collecting  $\tilde{v}_{dc}$  and  $\tilde{i}_o$  terms gives

$$\tilde{v}_{dc} \left( 1 - \frac{XPV_s}{V_{dc}(PV_{dc} - 1)} + \frac{RV_s}{V_{dc}(PV_{dc} - 1)} \right) = S\tilde{i}_o$$

and finally, the output voltage of the PV converter is expressed as

$$\tilde{v}_{dc} = \left[ \frac{SV_{dc}(PV_{dc} - 1)}{V_{dc}(PV_{dc} - 1) - XPV_s + RV_s} \right] \tilde{i}_o. \quad (2.43)$$

## 2.4 Energy Storage System

The energy storage system consists of battery packs, which stores excess energy generated by the PV and discharges when more power is required by the load. In grid-connected mode, the PV and the grid both supply power to the load and also for charging the battery storage. The direction of the current will be from the dc-bus to the battery and the bus voltage needs to be stepped down. Thus, a buck converter is required as an interface in this mode. If we want to sell any additional generated power or cut ac-load peaks or if the ac-grid is disconnected from the system by any fault, the battery changes its mode from charging to discharging and regulates the dc-bus voltage. In this mode, the interface works as a boost converter to step up the battery voltage. To control the flow of power in both directions, a bi-directional DC/DC converter is needed as an interface in this scenario. Consequently, the derivation for the bi-directional converter model working in boost mode (discharging) and buck mode (charging) has been addressed in the following subsections.

### 2.4.1 Bidirectional DC/DC Converter Model Working in Discharging Mode

In discharging mode, the converter steps up the battery-pack voltage to the dc-bus voltage and regulates it to its desired voltage level. However, this is only possible when the grid source is disconnected from the dc-microgrid, as such, this topology works only when the dc-microgrid is in an islanded mode. The boost converter circuit diagram and its control strategy are shown in Figure 2.2,  $v_B$  and  $v_{dc}$  are the battery pack voltage and output dc-bus voltages respectively.  $L$ ,  $C_1$  and  $C_2$  are the inductor and capacitor of the converter with their parasitic elements  $r_L$ ,  $r_{c1}$  and  $r_{c2}$ . The control strategy is implemented with an outer voltage control and an inner current control for faster response.

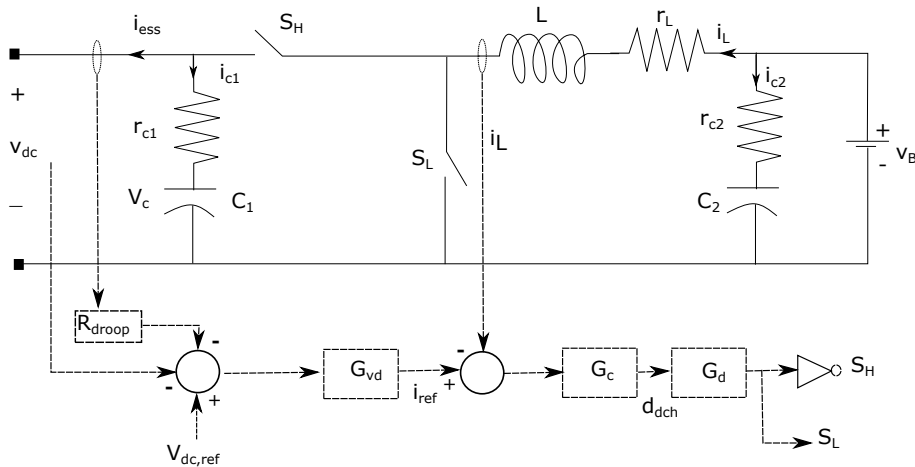


**Figure 2.2:** Topology of a bi-directional converter with discharging mode control.

In the control strategy shown in Figure 2.2,  $G_{vd}$  is the voltage controller,  $G_c$  is current controller and  $G_d$  is the PWM delay. Moreover, a droop control implementation, with a droop coefficient of  $R_{droop}$ , has been included to control the current sharing among converters connected in parallel on the dc-bus side. As in [12], the mathematical model for the boost converter is as follows:

When the switch  $S_L$  is closed and  $S_H$  is open, the ON-state equation of the converter is

$$C_1 \frac{dv_c}{dt} = -i_{ess} \quad (2.44)$$

where the direction of the current  $i_{ess}$  is positive from the battery to the dc-bus voltage.

$$v_B = r_L i_L + L \frac{di_L}{dt} \quad (2.45)$$

$$v_{dc} = v_c - i_{ess} r_{c1} \quad (2.46)$$

$$v_c = v_{dc} + i_{ess} r_{c1} \quad (2.47)$$

from (2.44)

$$C_1 \frac{d(v_{dc} + i_{ess} r_{c1})}{dt} = -i_{ess} \quad (2.48)$$

$$C_1 \frac{dv_{dc}}{dt} = -C_1 r_{c1} \frac{di_{ess}}{dt} - i_{ess}. \quad (2.49)$$

Similarly, the OFF-state equations, when  $S_L$  is open and  $S_H$  is closed

$$C_1 \frac{dv_c}{dt} = i_L - i_{ess} \quad (2.50)$$

$$v_B = r_L i_L + L \frac{di_L}{dt} + (i_L - i_{ess}) r_{c1} + v_c \quad (2.51)$$

$$v_{dc} = i_L r_{c1} - i_{ess} r_{c1} + v_c \quad (2.52)$$

$$v_c = i_{ess} r_{c1} - i_L r_{c1} + v_{dc}. \quad (2.53)$$

Combining (2.50) and (2.53)

$$C_1 \frac{dv_{dc}}{dt} = i_L - i_{ess} + C_1 r_{c1} \frac{di_L}{dt} - C_1 r_{c1} \frac{di_{ess}}{dt} \quad (2.54)$$

similarly, combining (2.51) and (2.53)

$$v_B = r_L i_L + L \frac{di_L}{dt} + v_{dc}. \quad (2.55)$$

The averaged equations of the bi-directional converter in boost mode considering on-off states can be expressed as

$$C_1 \frac{dv_{dc}}{dt} = -C_1 r_{c1} \frac{di_{ess}}{dt} - i_{ess} + (i_L + C_1 r_{c1} \frac{di_L}{dt})(1 - d_{dch}) \quad (2.56)$$

$$v_B = r_L i_L + L \frac{di_L}{dt} + (1 - d_{dch}) v_{dc} \quad (2.57)$$

$$v_{dc} = r_{c1} i_{ess} - r_{c1} i_L (1 - d_{dch}) + v_c \quad (2.58)$$

where  $d_{dch}$  is the duty cycle of the converter during discharging. Now, applying small signal analysis to (2.56)- (2.58), we have

$$sC_1 \tilde{v}_{dc} = \tilde{i}_{ess}(-C_1 r_{c1} - 1) + \tilde{i}_L(1 + sC_1 r_{c1})(1 - D_{dch}) - I_L \tilde{d}_{dch} \quad (2.59)$$

$$\tilde{v}_B = r_L \tilde{i}_L + sL \tilde{i}_L + (1 - D_{dch}) \tilde{v}_{dc} - V_{dc} \tilde{d}_{dch} \quad (2.60)$$

$$\tilde{v}_{dc} = r_{c1} \tilde{i}_{ess} - r_{c1} \tilde{i}_L (1 - D_{dch}) + r_{c1} I_L \tilde{d}_{dch} + \tilde{v}_c. \quad (2.61)$$

Relation between any two small signal perturbations can be derived as follows: considering  $\tilde{v}_B, \tilde{d}_{dch} = 0$ , we have from (2.59),(2.60)

$$sC_1 \tilde{v}_{dc} = (1 - D_{dch})(1 + sC_1 r_{c1}) \tilde{i}_L + \tilde{i}_{ess}(-C_1 r_{c1} - 1) \quad (2.62)$$

$$r_L \tilde{i}_L + sL \tilde{i}_L + (1 - D_{dch}) \tilde{v}_{dc} = 0 \quad (2.63)$$

$$\tilde{i}_L = \frac{-(1 - D_{dch}) \tilde{v}_{dc}}{r_L + sL} \quad (2.64)$$

inserting value of  $\tilde{i}_L$  in (2.62)

$$sC_1\tilde{v}_{dc} = \tilde{i}_{ess}(-C_1r_{c1} - 1) - \frac{(1 - D_{dch})^2(1 + sC_1r_{c1})\tilde{v}_{dc}}{r_L + sL} \quad (2.65)$$

$$\frac{\tilde{v}_{dc}}{\tilde{i}_{ess}} = \frac{(-C_1r_{c1} - 1)(r_L + sL)}{sC_1(r_L + sL) + (1 - D_{dch})^2(1 + sC_1r_{c1})} \quad (2.66)$$

$$Z_{out} = -\frac{\tilde{v}_{dc}}{\tilde{i}_{ess}} = -\frac{(-C_1r_{c1} - 1)(r_L + sL)}{sC_1(r_L + sL) + (1 - D_{dch})^2(1 + sC_1r_{c1})}. \quad (2.67)$$

Similarly, considering  $\tilde{v}_B, \tilde{i}_{ess} = 0$ , we have from (2.59),(2.60)

$$(r_L + sL)\tilde{i}_L + (1 - D_{dch})\tilde{v}_{dc} - V_{dc}\tilde{d}_{dch} = 0 \quad (2.68)$$

$$sC_1\tilde{v}_{dc} = \tilde{i}_L(1 + sC_1r_{c1})(1 - D_{dch}) - I_L\tilde{d}_{dch} \quad (2.69)$$

$$\tilde{i}_L = \frac{sC_1\tilde{v}_{dc} + I_L\tilde{d}_{dch}}{(1 + sC_1r_{c1})(1 - D_{dch})} \quad (2.70)$$

inserting  $\tilde{i}_L$  into (2.68), we have

$$\tilde{v}_{dc}((r_L + sL)sC_1 + (1 - D_{dch})^2(1 + sC_1r_{c1})) = \tilde{d}_{dch}(V_{dc}(1 + sC_1r_{c1})(1 - D_{dch}) - (r_L + sL)I_L)$$

$$\frac{\tilde{v}_{dc}}{\tilde{d}_{dch}} = \frac{(V_{dc}(1 + sC_1r_{c1})(1 - D_{dch}) - (r_L + sL)I_L)}{(r_L + sL)sC_1 + (1 - D_{dch})^2(1 + sC_1r_{c1})} = G_o. \quad (2.71)$$

Again, taking  $\tilde{v}_B, \tilde{d}_{dch}=0$ , from (2.59),(2.60) we get

$$r_L\tilde{i}_L + sL\tilde{i}_L + (1 - D_{dch})\tilde{v}_{dc} = 0 \quad (2.72)$$

$$sC_1\tilde{v}_{dc} = (1 - D_{dch})(1 + sC_1r_{c1})\tilde{i}_L + \tilde{i}_{ess}(-C_1r_{c1} - 1) \quad (2.73)$$

$$\tilde{v}_{dc} = \frac{(1 - D_{dch})(1 + sC_1r_{c1})\tilde{i}_L + \tilde{i}_{ess}(-C_1r_{c1} - 1)}{sC_1} \quad (2.74)$$

inserting  $\tilde{v}_{dc}$  in equation (2.72)

$$(r_L + sL)\tilde{i}_L + (1 - D_{dch})\frac{\tilde{i}_{ess}(-C_1r_{c1} - 1) + \tilde{i}_L(1 - D_{dch})(1 + sC_1r_{c1})}{sC_1} = 0 \quad (2.75)$$

$$((r_L + sL)sC_1 + (1 - D_{dch})^2(1 + sC_1r_{c1}))\tilde{i}_L = (1 - D_{dch})(1 + r_{c1}C_1)\tilde{i}_{ess} \quad (2.76)$$

$$\frac{\tilde{i}_L}{\tilde{i}_{ess}} = \frac{(1 - D_{dch})(1 + r_{c1}C_1)}{(r_L + sL)sC_1 + (1 - D_{dch})^2(1 + sC_1r_{c1})} = -A_{io}. \quad (2.77)$$

Similarly, taking  $\tilde{v}_s, \tilde{i}_o = 0$ , we have from (2.59),(2.60)

$$sC_1\tilde{v}_{dc} = (1 - D_{dch})(1 + sC_1r_{c1})\tilde{i}_L - I_L\tilde{d}_{dch} \quad (2.78)$$

$$r_L\tilde{i}_L + sL\tilde{i}_L + (1 - D_{dch})\tilde{v}_{dc} - V_{dc}\tilde{d}_{dch} = 0. \quad (2.79)$$

From (2.78), we have

$$\tilde{v}_{dc} = \frac{(1 - D_{dch})(1 + sC_1r_{c1})\tilde{i}_L - I_L\tilde{d}_{dch}}{sC_1}. \quad (2.80)$$

Substituting value of  $\tilde{v}_{dc}$  in (2.79)

$$(r_L + sL)\tilde{i}_L + (1 - D_{dch})\frac{\tilde{i}_L(1 + sC_1r_{c1})(1 - D_{dch}) - I_L\tilde{d}}{sC_1} - V_{dc}\tilde{d}_{dch} = 0. \quad (2.81)$$

$$((r_L + sL)sC_1 + (1 - D_{dch})^2(1 + sC_1r_{c1}))\tilde{i}_L - (I_L(1 - D_{dch}) + sV_{dc}C_1)\tilde{d}_{dch} = 0 \quad (2.82)$$

$$\frac{\tilde{i}_L}{\tilde{d}_{dch}} = \frac{I_L(1 - D_{dch}) + sV_{dc}C_1}{(r_L + sL)sC_1 + (1 - D_{dch})^2(1 + sC_1r_{c1})} = G_{id}. \quad (2.83)$$

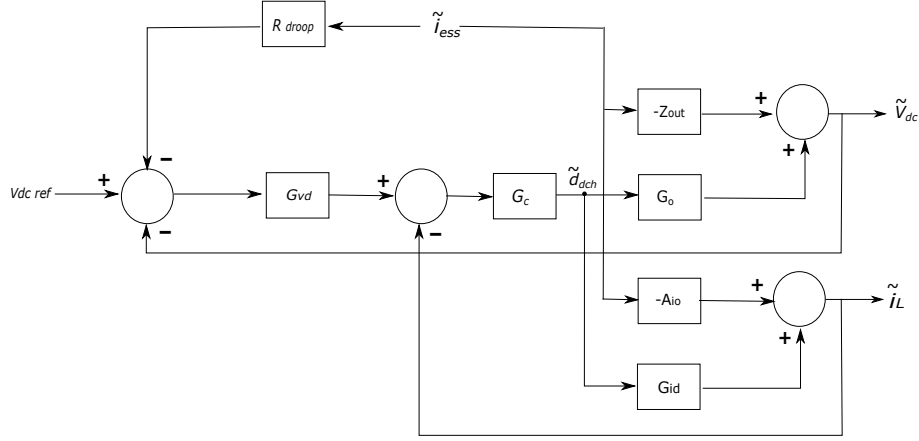


**Figure 2.3:** Small signal control diagram with droop controller.

Using a signal flow graph analysis and the Mason's Gain Formula (MGF) from [13], the relation between dc-bus voltage and current of the bi-directional DC/DC converter is expressed as

$$\frac{\tilde{v}_{dc}}{\tilde{i}_{ess}} = \frac{Z_{out}(1 + G_c G_{id}) + G_c G_o (A_{io} - R_{droop} G_{vd})}{1 + G_{vd} G_c G_o + G_c G_{id}}. \quad (2.84)$$

### 2.4.2 Bidirectional DC/DC Converter Model Working in Charging Mode

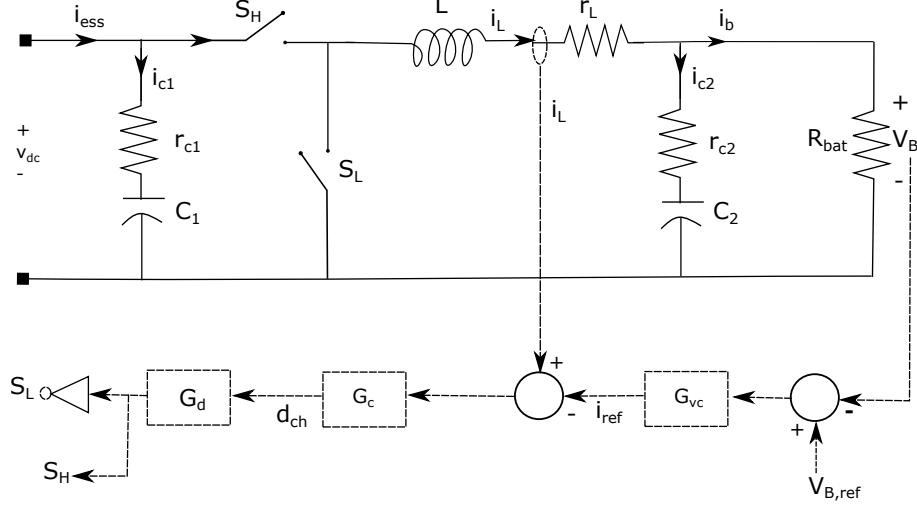


**Figure 2.4:** Topology of a bi-directional converter with charging mode control.

In charging mode, the power flow direction is from the dc-bus line to the battery and the bidirectional DC/DC converter acts a buck converter that steps down the dc-bus voltage to the battery-pack voltage and regulates it to its desired value. Similar to [12], the mathematical model in this case for a buck converter is derived as follows: The average state-space equations of the buck converter shown in Figure 2.4 can be expressed as

$$d_{ch}v_{dc} = L \frac{di_L}{dt} + r_L i_L + v_B \quad (2.85)$$

$$i_{ess} = C_1 \frac{dv_{dc}}{dt} + d_{ch}i_L \quad (2.86)$$

$$i_L = \frac{v_B}{R_{bat}} + C_2 \frac{dv_B}{dt} \quad (2.87)$$

where,  $d_{ch}$ , is the duty cycle of the converter during charging;  $v_{dc}$ ,  $i_{ess}$  are voltage and current on the dc-bus side while  $v_B$ ,  $i_b$  voltage and current on the battery side respectively.  $L$ ,  $C_1$ ,  $C_2$ ,  $r_L$ ,  $r_{c1}$  and  $r_{c2}$  are the same as specified in (2.4.1) the bi-directional converter working as in discharging mode.

To regulate the battery pack voltage, the converter changes its duty cycle based on the control strategy applied. Using the voltage and inner current control, the relationship between the duty cycle and the output voltage is expressed as

$$d_{ch} = G_c(G_{vc}(v_{Bref} - v_B) - i_L). \quad (2.88)$$

where,  $v_{Bref}$ , is battery reference voltage and  $G_{vc}$ ,  $G_c$  are proportional-integral (PI) controller gains of the voltage and current during charging mode respectively. Applying small signal analysis to (2.86) and (2.88) and changing them to frequency domain

$$V_{dc}\tilde{d}_{ch} + D_{ch}\tilde{v}_{dc} = (sL + r_L)\tilde{i}_L + \tilde{v}_B \quad (2.89)$$

$$\tilde{i}_{ess} = sC_1\tilde{v}_{dc} + \frac{D_{ch}}{R_{bat}}\tilde{v}_B + sC_2\tilde{d}_cV_B + sC_2D_{ch}\tilde{v}_B \quad (2.90)$$

$$\tilde{d}_{ch} = G_c(G_{vc}(v_{Bref} - \tilde{v}_B) - \tilde{i}_L). \quad (2.91)$$

Taking the relationship between any two small-signal perturbations, the small-signal state equations are divided into blocks as follows:

For  $\tilde{i}_L$  and  $\tilde{d}_{ch}$  equal to zero in (2.89)

$$B_{io}(s) = \frac{\tilde{v}_B}{\tilde{v}_{dc}} = D_{ch}. \quad (2.92)$$

For  $\tilde{v}_{dc}$  and  $\tilde{i}_L$  equals zero in (2.89)

$$F_{vd}(s) = \frac{\tilde{v}_B}{\tilde{d}_{ch}} = V_{dc}. \quad (2.93)$$

For  $\tilde{i}_L$  and  $\tilde{d}_{ch}$  equal to zero in (2.90)

$$D_{io} = \frac{\tilde{i}_{ess}}{\tilde{v}_{dc}} = s(C_1 + C_2D_{ch}^2) + \frac{D_{ch}^2}{R_{bat}}. \quad (2.94)$$

For  $\tilde{i}_L$  and  $\tilde{v}_{dc}$  equal to zero in (2.90)

$$F_{id}(s) = \frac{\tilde{i}_{ess}}{\tilde{d}_{ch}} = s(C_2V_B + C_2V_{dc}D_{ch}) + \left(\frac{V_B}{R_{bat}} + \frac{D_{ch}}{R_{bat}}\right). \quad (2.95)$$

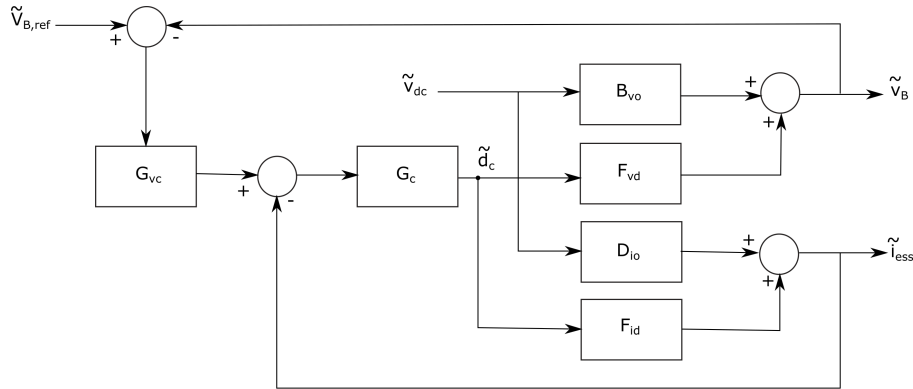


**Figure 2.5:** Small signal control diagram (charging).

Using a signal flow graph analysis and MGF, the relationship between the dc-bus current and voltage across the input terminal of the bi-directional DC/DC converter is expressed as

$$\frac{\tilde{v}_{dc}}{\tilde{i}_{ess}} = \frac{1 + G_{vc}G_cF_{vd} + F_{id}G_c}{D_{io}(1 + G_{vc}G_cF_{vd}) - B_{vo}G_{vc}G_c}. \quad (2.96)$$

## 2.5 Modelling of Loads

### 2.5.1 Resistive Loads

Resistive loads are electrical loads that convert electrical energy into thermal energy and dissipate it in the form of heat. These type of loads show a linear V-I relationship, i.e when the voltage increases, the load current increases or vice versa. Thus, resistive loads have a positive resistance increment which improves the stability of the system.

### 2.5.2 Constant Power Load (CPL) Model

In a CPL, the load power remains constant while the voltage and current show nonlinear V-I characteristics; i.e while the dc-bus voltage increases, the load current decreases or vice-versa as depicted in Figure 2.6. Consequently, as explained in 2.2, a negative resistance characteristic occurs in this type of loads.

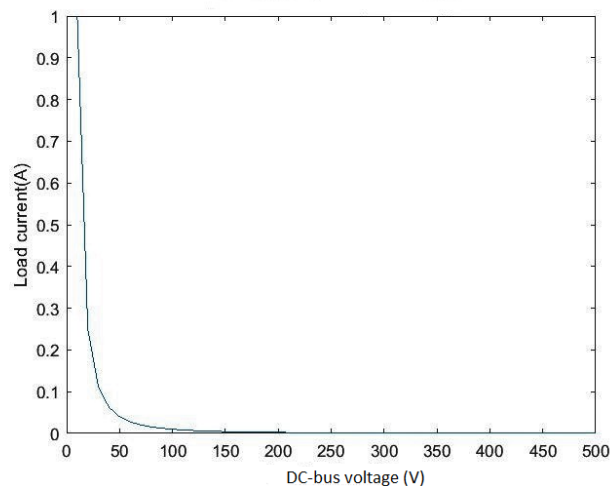


**Figure 2.6:** Voltage  $v$ /s Current characteristic for a CPL.

CPL models are usually connected to a bus through power electronic converters which tightly regulate the output voltage as is shown in Figure 2.7. When the controller in the control strategy has a fast response, the change in the bus voltage can be ignored and it can be taken as CPL at the input of the buck converter. The power consumed by the load will be

$$p = v_{dc} \cdot i_{load} \quad (2.97)$$

where,  $v_{dc}$ ,  $i_{load}$  and  $p$  are input voltage, input current and rated power of the converter respectively.

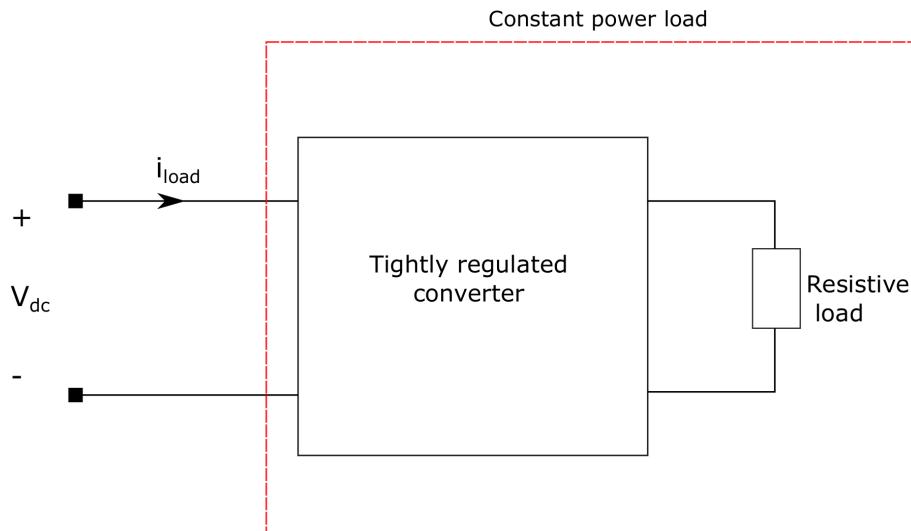


**Figure 2.7:** A CPL consisting of a tightly regulated converter and a resistive load.

Applying small signal analysis, the impedance at the input terminal of the converter will be

$$0 = \tilde{v}_{dc} I_{load} + \tilde{i}_{load} V_{dc} \quad (2.98)$$

$$\frac{\tilde{v}_{dc}}{\tilde{i}_{load}} = -\frac{V_{dc}}{I_{load}}$$

$$Z_{CPL} = -\frac{V_{dc}}{I_{load}} = -\frac{(V_{dc})^2}{P} \quad (2.99)$$

## 2.6 Grid Source Interface

A converter in the ac-grid side rectifies the ac voltage from the grid to a dc-bus voltage and maintains it fixed within a specified range. It also transfers power into the dc-grid and maintains overall power balance. Furthermore, when excess power is generated by PV source, it works as dc to ac converter and feeds back the power to the ac-grid. Thus, a VSC which transfers power in both directions is required as an interface. A two-level converter topology being simple to implement has been taken for the study and its mathematical model is derived.

### 2.6.1 Voltage Source Converter Model

An equivalent model representing a VSC connecting the ac side source to the dc-bus line via filter inductor and resistor is shown in Figure 2.8



2.9, the control strategy for the steady-state equation along the d-axis is expressed as

$$v_d = -G_i(i_{dref} - i_d) + \omega_g Li_q + e_d \quad (2.102)$$

where  $G_i$  is the inner current controller and  $i_{dref}$  is a d-axis reference current. In the double loop with inner current control, the outer dc voltage controller calculates the reference value of current which is the input to the d-axis inner current loop. Similarly, the steady state equation along the q-axis is expressed as

$$v_q = -G_i(i_{qref} - i_q) - \omega_g Li_d + e_q \quad (2.103)$$

where  $i_{qref}$  is a q-axis reference current. As only active power is assumed to be transferred (unity power factor) from the ac-source to the dc-bus,  $i_{qref}$  will be zero. Substituting values of  $e_d, e_q$  from (2.102),(2.103) into (2.100),(2.101), we have

$$e_d = L \frac{di_d}{dt} + ri_d - \omega_g Li_q - G_i(i_{dref} - i_d) + \omega_g Li_q + e_d \quad (2.104)$$

$$L \frac{di_d}{dt} + ri_d = G_i(i_{dref} - i_d) \quad (2.105)$$

$$e_q = L \frac{di_q}{dt} + ri_q + \omega_g Li_d - G_i(i_{qref} - i_q) + \omega_g Li_d + e_q \quad (2.106)$$

$$L \frac{di_q}{dt} + ri_q = G_i(i_{qref} - i_q). \quad (2.107)$$

Applying Laplace transform to (2.105),(2.107)

$$(sL + r)i_d = G_i(i_{dref} - i_d) \quad (2.108)$$

$$(sL + r)i_q = G_i(i_{qref} - i_q). \quad (2.109)$$

Applying a small perturbation and using small signal analysis to above equations, we have

$$(sL + r)\tilde{i}_d = G_i(\tilde{i}_{dref} - \tilde{i}_d) \quad (2.110)$$

$$\tilde{i}_d = \frac{(\tilde{i}_{dref} - \tilde{i}_d)G_i}{sL + r} \quad (2.111)$$

and

$$(sL + r)\tilde{i}_q = G_i(\tilde{i}_{qref} - \tilde{i}_q) \quad (2.112)$$

$$\tilde{i}_q = \frac{(\tilde{i}_{qref} - \tilde{i}_q)G_i}{sL + r}. \quad (2.113)$$

Based on the power balance between two sides of the VSC considering amplitude invariant Clarke transform

$$\frac{3}{2}(v_d i_d + v_q i_q) = v_{dc} i'_{dc} = v_{dc} (C_{dc} \frac{dv_c}{dt} + i_{dc}). \quad (2.114)$$

As VSC adopts a grid-voltage oriented control that assumes the d-axis is perfectly aligned along with the point of common-coupling (PCC) voltage, with this assumption  $v_q = 0$ . Moreover, the phase-locked loop (PLL) in the controller tracks the phase  $a$  voltage at the PCC. Thus, (2.114) is further reduced to

$$\frac{3}{2}(v_d i_d) = v_{dc} i'_{dc} = v_{dc} (C_{dc} \frac{dv_c}{dt} + i_{dc}). \quad (2.115)$$

On the dc-side

$$v_{dc} = v_c + i_c r_c$$

$$v_{dc} = v_c + C_{dc} \frac{dv_c}{dt} r_c \quad (2.116)$$

where  $r_c$  is the parasitic resistance of the dc-side capacitor. Applying Laplace transform to (2.116)

$$v_{dc}(s) = v_c(s) + sC_{dc}r_c v_c(s). \quad (2.117)$$

In small signal

$$\tilde{v}_{dc}(s) = \tilde{v}_c(s) + sC_{dc}r_c \tilde{v}_c(s). \quad (2.118)$$

Equation (2.115) in small signal form and frequency domain

$$\frac{3}{2}(\tilde{v}_d I_d + V_d \tilde{i}_d) = sV_{dc}C_{dc}\tilde{v}_c(s) + V_{dc}\tilde{i}_{dc}(s) + \tilde{v}_{dc}(s)I_{dc}. \quad (2.119)$$

Substituting  $\tilde{v}_c$  from (2.118)

$$\frac{3}{2}(\tilde{v}_d I_d + V_d \tilde{i}_d) = sV_{dc}C_{dc} \frac{\tilde{v}_{dc}(s)}{1 + sC_{dc}r_c} + V_{dc}\tilde{i}_{dc}(s) + \tilde{v}_{dc}(s)I_{dc} \quad (2.120)$$

$$\frac{3}{2}(\tilde{v}_d I_d + V_d \tilde{i}_d) = sV_{dc}C_{dc} \frac{\tilde{v}_{dc}(s)}{1 + sC_{dc}r_c} + V_{dc}\tilde{i}_{dc}(s) + \tilde{v}_{dc}(s)I_{dc}. \quad (2.121)$$

Using superposition theorem, relation between any two perturbations can be obtained by neglecting perturbation from other components in (2.121). First, the relation between  $\tilde{v}_{dc}$  and  $\tilde{i}_d$  is obtained by setting  $\tilde{v}_d$  and  $\tilde{i}_{dc} = 0$  as in [14]

$$\frac{3}{2}(V_d \tilde{i}_d) = sV_{dc}C_{dc} \frac{\tilde{v}_{dc}(s)}{1 + sC_{dc}r_c} + \tilde{v}_{dc}I_{dc} \quad (2.122)$$

$$\frac{\tilde{v}_{dc}}{\tilde{i}_d} = \frac{3}{2} \frac{V_d(1 + sC_{dc}r_c)}{sC_{dc}V_{dc} + I_{dc}(1 + sC_{dc}r_c)} = G_1. \quad (2.123)$$

Now, applying Laplace transform and inserting  $\tilde{v}_d$  and  $\tilde{i}_d = 0$  in (2.121), relation between  $\tilde{v}_{dc}$  and  $\tilde{i}_{dc}$  is

$$sV_{dc}C_{dc} \frac{\tilde{v}_{dc}(s)}{1 + sC_{dc}r_c} + V_{dc}\tilde{i}_{dc} + \tilde{v}_{dc}I_{dc} = 0 \quad (2.124)$$

$$\frac{\tilde{v}_{dc}}{\tilde{i}_{dc}} = -\frac{V_{dc}(1 + sC_{dc}r_c)}{sC_{dc}V_{dc} + I_{dc}(1 + sC_{dc}r_c)} = G_2. \quad (2.125)$$

Similarly taking  $\tilde{i}_{dc}$  and  $\tilde{v}_d=0$ , relation between  $\tilde{v}_{dc}$  and  $\tilde{v}_d$  is

$$\frac{3}{2}(\tilde{v}_d I_d) = sV_{dc}C_{dc} \frac{\tilde{v}_{dc}(s)}{1 + sC_{dc}r_c} + \tilde{v}_{dc}I_{dc} \quad (2.126)$$

$$\frac{\tilde{v}_{dc}}{\tilde{v}_d} = \frac{3}{2} \frac{I_d(1 + sC_{dc}r_c)}{I_{dc}(1 + sC_{dc}r_c) + sC_{dc}V_{dc}} = G_3. \quad (2.127)$$

## 2.6.2 Control Parameter Selection

In the synchronous reference frame control, the outer voltage controller and inner current controller parameters have to be designed based on the system parameters. The cross-coupling term due to the input ac inductor is compensated by including a decoupling loop in the current controller. Thus, the current control parameters should be dependent on the filter inductor and resistance for decoupling.

Re-arranging (2.108), the equation will be written as

$$\frac{i_d}{i_{dref}} = \frac{G_i}{Ls + r + G_i} = \frac{k_{ip}s + k_{ii}}{Ls^2 + (r + k_{ip})s + k_{ii}} \quad (2.128)$$

$$\frac{i_d}{i_{dref}} = \frac{k_{ip}(s + \frac{k_{ii}}{k_{ip}})}{Ls(s + \frac{r}{L}) + k_{ip}(s + \frac{k_{ii}}{k_{ip}})} \quad (2.129)$$

where  $k_{ip}$  and  $k_{ii}$  are proportional and integral gains of the current controller respectively. If the ratio of  $\frac{r}{L}$  and  $\frac{k_{ii}}{k_{ip}}$  are kept equal, the expression on the denominator could be combined and overall expression simplified further resulting in pole-zero cancellation. As a result, the current controller transfer function is reduced to a linear one and its bandwidth could be determined.

$$\frac{i_d}{i_{dref}} = \frac{\frac{k_{ip}}{L}}{s + \frac{k_{ip}}{L}} \quad (2.130)$$

where  $\frac{k_{ip}}{L}$  is bandwidth of the current controller. In [15], it is recommended that the bandwidth should be  $\leq 0.2$  times the switching frequency. Thus,  $k_{ip}$  can be calculated once an appropriate bandwidth is selected. Furthermore, the  $k_{ii}$  is calculated from the ratio  $\frac{r}{L} = \frac{k_{ii}}{k_{ip}}$ .

As explained above and shown in Figure 2.9, the error of  $(v_{dc}^{ref} - v_{dc} - R_{dr}i_{dc})$  is given as input. The dc voltage controller that would make the closed loop dynamics dependent on the steady state voltage. To consider the dc-link dynamics when energy stored on the dc-link capacitor, a PI controller operating on the error  $((V_{dc}^{ref})^2 - v_{dc})^2 - R_{dr}i_{dc}V_{ref}$  could be used [15]. Thus, the reference current on the d-component,  $i_{ref}$  is calculated from the reference power,  $P_{ref}$  as

$$i_{ref} = \frac{G_{vi}((V_{dc}^{ref})^2 - v_{dc}^2 - R_{dr}i_{dc}V_{dc}^{ref})}{E_g} \quad (2.131)$$

where  $E_g = \sqrt{E_d^2 + E_q^2}$ .

The small signal analysis of (2.131) will be

$$i_{ref}^{\sim} = \frac{2V_{dc}}{E_g} G_{vi}(\tilde{v}_{dc}^{ref} - \tilde{v}_{dc} - 0.5R_{dr}\tilde{i}_{dc}) \quad (2.132)$$

$$i_{ref}^{\sim} = G_{gain} G_{vi}(-\tilde{v}_{dc} - 0.5R_{dr}\tilde{i}_{dc}) \quad (2.133)$$

where  $G_{gain} = \frac{2V_{dc}}{E_g}$  and  $\tilde{v}_{dc}^{ref} = 0$ .

All the expressions found above can be interconnected as shown in Figure 2.10

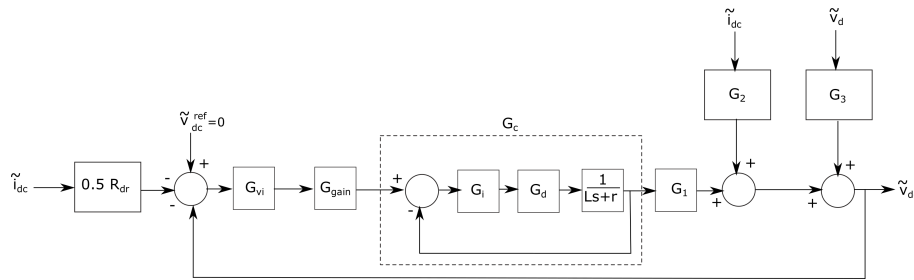


**Figure 2.10:** Small-signal model for control of VSC.

where,  $G_{vi}$ , is the dc side voltage regulator,  $G_i$  is the current controller,  $G_d$  is the PWM delay and  $R_{dr}$  is the droop co-efficient. A transfer function relating the output rectified voltage and output current of the VSC is expressed as

$$\frac{\tilde{v}_{dc}}{\tilde{i}_{dc}} = \frac{R_{dr}G_{gain}G_{vi}G_cG_1 - G_2}{1 + G_{vi}G_cG_1}. \quad (2.134)$$

## 2.7 Stability Analysing Techniques

### 2.7.1 Eigenvalue Analysis

There are different approaches to analyzing the stability of a system. An eigenvalue based analysis is one approach where the system's closed loop poles are calculated to identify the risk for resonance interactions [16]. This approach is more effective for investigating the system stability as the poles of the closed loop are calculated directly. However, it could be tedious to calculate the poles of a large system and a new state-space model would be required if there are any changes on the system's model. Moreover, it is difficult with this approach to study the contribution of each subsystem on the stability of the overall system as it gives little information.

### 2.7.2 Nyquist Stability Criterion

The Nyquist stability criterion approach depends on frequency domain analysis. This method focuses on the feedback of the closed-loop system of the interconnection of two subsystems represented by their equivalent impedance or admittance. As a consequence, the stability of the interconnected system is studied using the open-loop transfer function of the entire system [16]. With this approach, the stability of the overall system could be analysed with different control parameters. However, the contribution of each subsystem on the stability of the interconnected system can not be clearly indicated. This technique will be used in this paper to study the impact of different control parameters or system operating points on the stability of the overall system.

### 2.7.3 Passivity Analysis of the System

An impedance-based stability method which is used to study the contribution of individual subsystems on the overall stability is the passivity approach. It states

that a transfer function,  $T(s)$  representing the impedance or admittance of one subsystem is defined as passive, if it satisfies two conditions [17]:

1.  $T(s)$  is stable.
2.  $\text{Re}\{T(j\omega)\} \geq 0, \forall \omega \geq 0$ .

Which implies that for a system to be passive, it should first be stable (this can be determined from the pole-zero map of the transfer function, where all poles must be to the left of the s-plane). Second, the transfer function has a non-negative real part for all frequencies. The interconnected system might not fulfil the passivity behaviour for the entire frequency range. These non-passive regions in the individual converters can make the overall system less passive, thereby reducing system stability. Which is why passivity analysis is needed along with Nyquist criteria to study the system.



# 3

## System Modelling

This chapter discusses the methodology regarding how the dc-microgrid system is modelled based on the derivations in the previous chapter. Section 3.1 explains the final model derivation for each of the subsystems: impedance of the PV converter, admittance of the energy storage system and impedance of the VSC. Section 3.2 explains the simulation models; Section 3.3 discusses the verification of mathematically derived impedance models with the simulation models developed using the same parameters. Furthermore, Section 3.4 checks the verification of passivity criteria for each of the individual subsystems and finally in Section 3.5, the simplified dc-microgrid structure is discussed.

### 3.1 Modelling of DC-microgrid Analytically

The overall dc-microgrid system has PV panels for energy generation, battery pack for storage, a VSC which feeds power from the grid to maintain a constant dc-bus voltage and also fulfill additional power requirement and load demand. Each of these sub units is modelled individually and combined to study the overall system. Equivalent impedance/admittance models are derived for each of the sub units, considering appropriate power converter models.

#### 3.1.1 Impedance Model on PV side Converter

In the real system on the PV side, solar panels are clustered in units, which are then connected to solar string optimizers (SSO). These optimizers are MPPT controllers combined with boost converters. MPPT is used to extract maximum power depending on the varying solar irradiance levels.

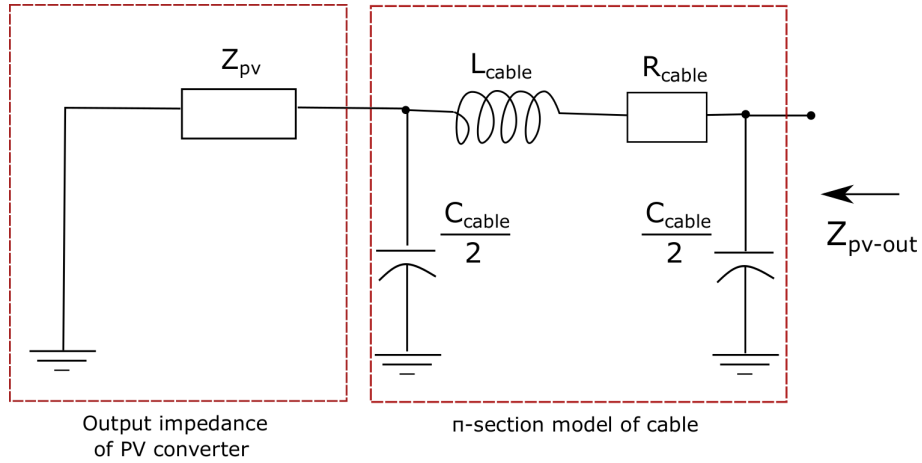
In the impedance model derivation, the output of PV is considered as a current source. Taking the dc-bus voltage of the boost converter as feedback and input voltage as reference for maximum power production, the duty cycle then is determined. The final expression for input impedance of the PV unit can be found from (2.43), which is expressed as

$$Z_{pv} = \frac{SV_{dc}(PV_{dc} - 1)}{V_{dc}(PV_{dc} - 1) - XPV_s + RV_s}. \quad (3.1)$$

**Table 3.1:** Cable parameters [2], [3].

Type of DC line	Cable length(km)	r( $\Omega$ /km)	L (mH/km)	C ( $\mu$ F/km)
Cable PV AWL	0.047	0.641	0.21	0.45
Cable PV SB	0.027	0.641	0.21	0.45
Cable b/w PV AWL and SB	0.065	0.125	0.13	0.45

The PV panels in the real system are located in two building roofs, SB3 and AWL. There are long cables coming from the roofs to the basement and they are required to be studied for the effect on stability; other cables are very short compared with these and have been ignored for investigation. The cable on the PV side has been added to the model as a pi-section (lumped form) and the values are taken as in Table 3.1.


**Figure 3.1:** PI model of cables between the PV converter and DC-bus line.

The length of cables from SB3 building to the DC switch-gear is 27 m and from AWL building to the switch-gear is 47 m. The cable length between the two building is 65 m. Considering the cable impedance, the final expression for input impedance of the PV system can be expressed as

$$Z_{pv-out} = Z_{pv} // \frac{2}{sC_{cable}} + sL_{cable} + R_{cable} // \frac{2}{sC_{cable}}. \quad (3.2)$$

In admittance form

$$Y_{pv-out} = \frac{1}{Z_{pv-out}}. \quad (3.3)$$

### 3.1.2 Admittance Model of CPL

From (2.99), load admittance of the CPL can be expressed as

$$Y_{CPL} = \frac{1}{Z_{CPL}} \quad (3.4)$$

in order to be taken together with the other system admittances in the overall analysis.

### 3.1.3 Admittance Model of Energy Storage Converter

In grid-connected mode, the dc-bus voltage is regulated by the inverter and the battery can only change the current input to the converter. Thus, the energy storage is designed as a current source and the battery works in charging mode. In the charging mode of the energy storage, the bi-directional DC/DC converter works as in buck mode. As a result, the input admittance of the converter is an appropriate model to be taken in this subsystem. Bi-directional DC/DC converter working as a buck converter (charging mode) has been derived in the theory section. Therefore, input admittance of the converter is derived from (2.96).

$$Y_{storage} = \frac{\tilde{i}_{ch}}{\tilde{v}_{dc}} = \frac{D_{io}(1 + G_{vd}G_cF_{vd}) - B_{vo}G_vG_c}{1 + G_{vd}G_cF_{vd} + F_{id}G_c}. \quad (3.5)$$

### 3.1.4 Impedance Model of Voltage Source Converter

In the VSC, the input impedance is determined from the dc-side of the converter. Incoming three phase voltages and currents are converted into equivalent d-q system for easy control of the converter. Applying power balance on both sides of the VSC and taking only active power from the grid, the input impedance of the VSC in (2.134) is expressed as

$$Z_{vsc} = -\frac{\tilde{v}_{dc}}{\tilde{i}_{dc}} = \frac{R_{dr}G_{gain}G_vG_cG_1 - G_2}{1 + G_vG_cG_1}. \quad (3.6)$$

## 3.2 Modelling of DC-microgrid in Simulink

### 3.2.1 PV Model

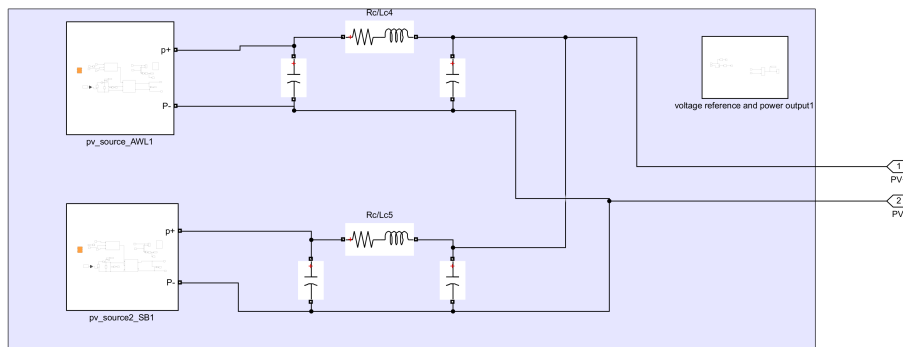


**Figure 3.2:** PV model for panels located at AWL and SB3.

Figure 3.2 shows the PV converter setup in Simulink for the two buildings AWL and SB3 where the solar panels are located. To include the cable effects, the cable parameters are lumped together in pi-section.

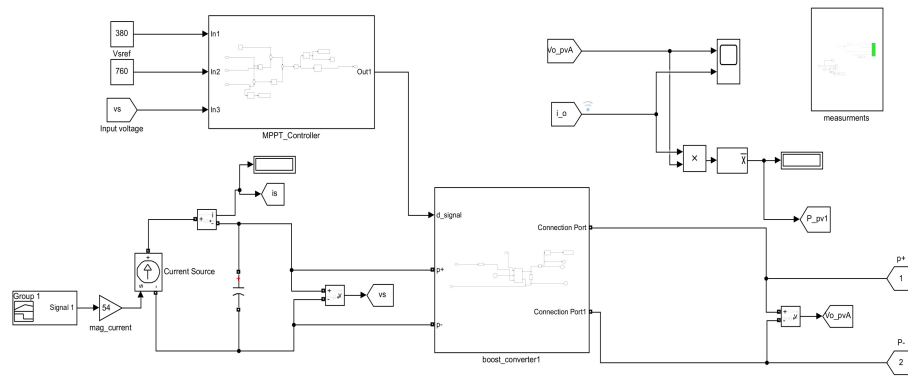


**Figure 3.3:** PV model AWL building.

Figure 3.3 shows the converter circuit for the PV system. As seen in the figure, the PV panel is replaced by a current source. For a fixed power level from the current source, a voltage reference is provided to the controller, this reference voltage is the optimum point where peak power is obtained. The controller takes this reference, output and input voltage from the converter as its input parameters and generates the duty cycle to control the switch in the boost converter.

### 3.2.2 Energy Storage Model

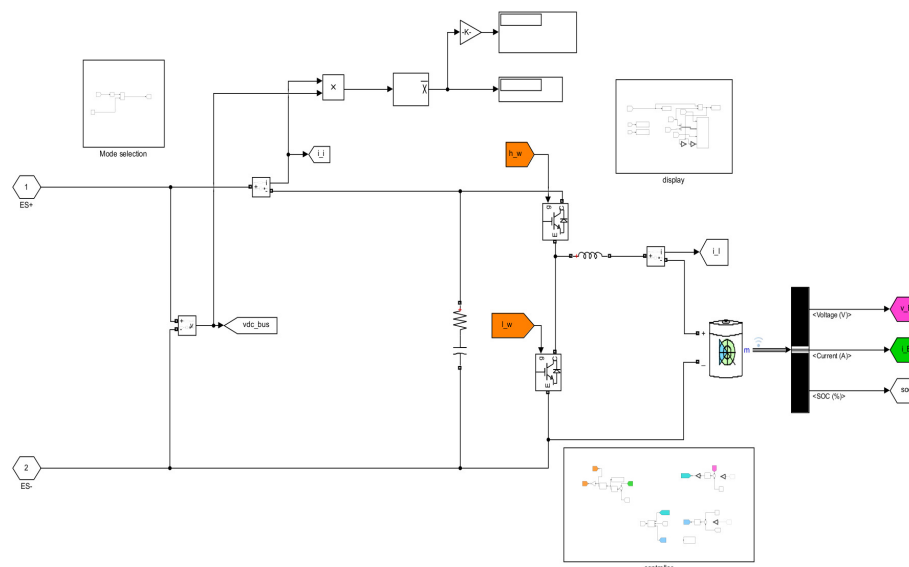


**Figure 3.4:** Simulation model for the energy storage system.

Figure 3.4 shows the energy storage converter circuit. As it can be seen, the circuit contains two switches according to the topology of the bi-directional converter. The high voltage side is at 760 V level while at the battery side the nominal voltage is 380 V.

The control for the charging and discharging modes of operation is shown in Figure

3.5. During the charging state, the output voltage on the battery side is compared with the reference battery voltage and is fed to a voltage (PI) controller. This generates a reference current that is passed to the inner current (PI) controller and generates switching pulses for the two switches. For the discharge case, the voltage controller is implemented with droop control for power-sharing between converters connected on the same side. The droop coefficient will be chosen which ensures that the output voltage to be maintained within . Depending on the mode that the converter operates, the reference current to the inner current controller is adjusted.

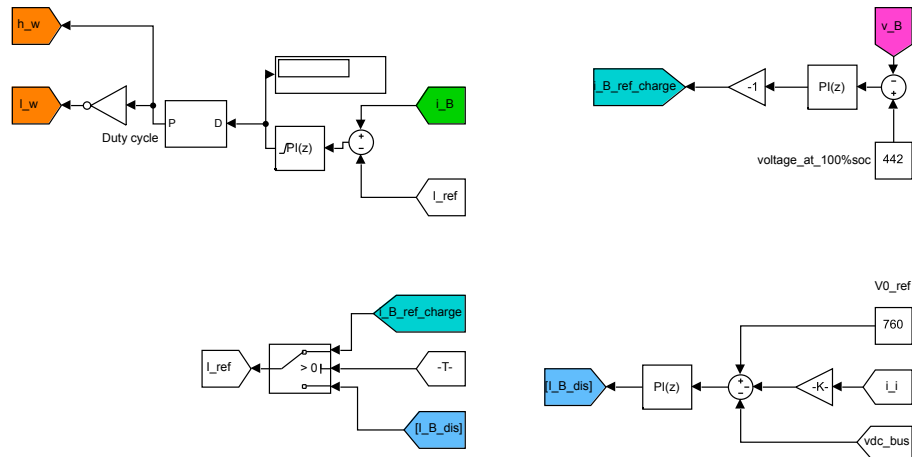


Figure 3.5: Energy storage control model (charging and discharging).

### 3.2.3 VSC Model

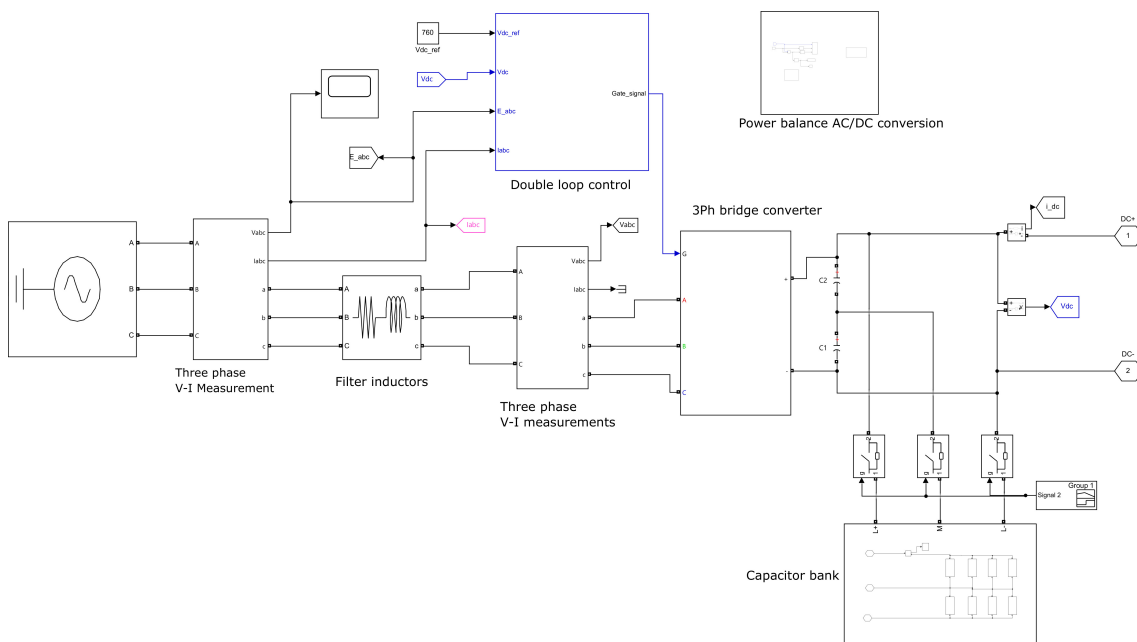
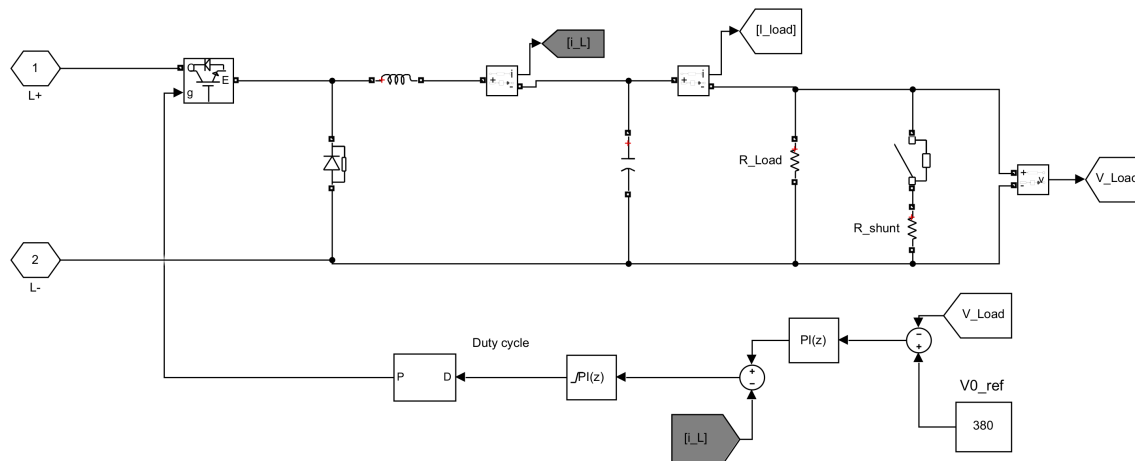


Figure 3.6: Simulation model of the VSC.

Figure 3.6 shows the VSC model. The ac grid supplies 400 VAC @50 Hz to the VSC which converts it to 760 V. A droop based control strategy is implemented to keep dc bus voltage within permissible limits of while maintaining the power balance of the overall system.

### 3.2.4 CPL Model



**Figure 3.7:** Simulation model of the CPL consisting of a tightly regulated converter and a resistive load.

Figure 3.7 is the simulation model of a CPL which consists of a tightly regulated buck converter that maintains a constant voltage at the load side along with a resistive load.

## 3.3 Verification of Impedance Models

For verifying the derived impedance models, a frequency sweep is performed for a specified frequency range in the impedance expression derived. The resultant magnitude and phase for the frequency sweep are compared with the results from simulation. In the simulation model, a constant magnitude variable frequency sinusoidal alternating voltage is superimposed with a dc voltage. The magnitude is 38 V which is 5% of the dc-bus voltage. The current response from the converter is obtained and using Fast Fourier Transform (FFT), both voltage and current perturbations are extracted from the signal. The input impedance magnitude of the model is obtained by dividing voltage perturbation with current perturbation. Finally, both the magnitude and the phase of impedance of the converter is compared with the derived analytical model.

### 3.3.1 Verification of VSC Impedance Model

**Table 3.2:** Rated values of VSC.

$V_{abc}$	AC line voltage	400 V
$P_{vsc}$	VSC rated power	28 kW
$f$	AC frequency	50 Hz
$L_{vsc}$	Filter inductance of VSC	3 mH
$r_{vsc}$	Filter resistance of VSC	0.05 $\Omega$
$C_{dc}$	DC side capacitance	4700 $\mu$ F
$V_{dc}$	Output DC voltage	760 V
$V_{dcm}$	Minimum output DC voltage	720 V
$f_v, f_c$	Bandwidth of voltage and current controller(Hz)	10 Hz, 100 Hz
$k_{pv}$	Proportional gain of voltage controller	$C_{dc}(2\pi f_v)$
$k_{iv}$	Integral gain of voltage controller	$C_{dc}(2\pi f_v)^2$
$k_{pi}$	Proportional gain of current controller	$L_{vsc}2\pi f_c$
$k_{ii}$	Integral gain of voltage controller	$r_{vsc}2\pi f_c$
$R_{droop}$	Droop gain	0.04
$f_{sw}$	Switching frequency	5 kHz
$C_{bank}$	Capacitor bank capacitance	7 mF

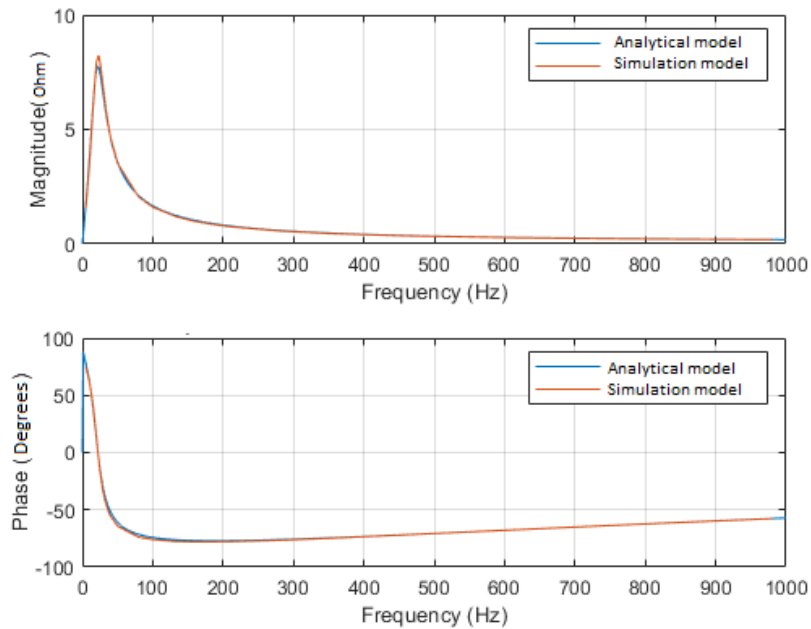


**Figure 3.8:** Impedance verification of VSC for analytical and simulation models for various frequencies.

Figure 3.8 is the impedance plot for the VSC, in the magnitude part, the peak value of the impedance is at lower frequency in both the theoretical and simulation plot

and it decreases with increasing frequency, this peak is due to controller parameters which are dominant at lower frequency. The phase plot changes from positive to a negative phase around the same frequency with the peak magnitude of the impedance.

### 3.3.2 Verification of PV Impedance Model

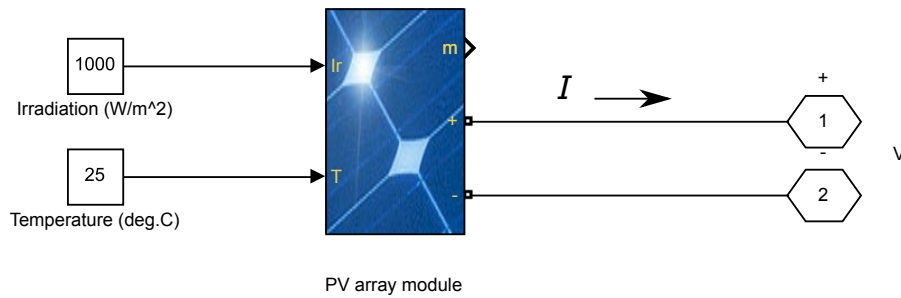


**Figure 3.9:** PV array module from Simulink used for specifying reference voltage[1].

For a specific irradiance and temperature, voltage and current are specified from the PV panel to generate maximum power. For irradiance of  $1000 \text{ W/m}^2$  and operating temperature of  $25^\circ\text{C}$ , a PV array of 7 modules and 3 strings is selected based on the converter rating. Thus, the maximum power at this operating point of the PV is around 6.7 kW and the corresponding reference voltage to maintain this power level is 380 V with a current of 18 A, as can be observed from Figure 3.10.

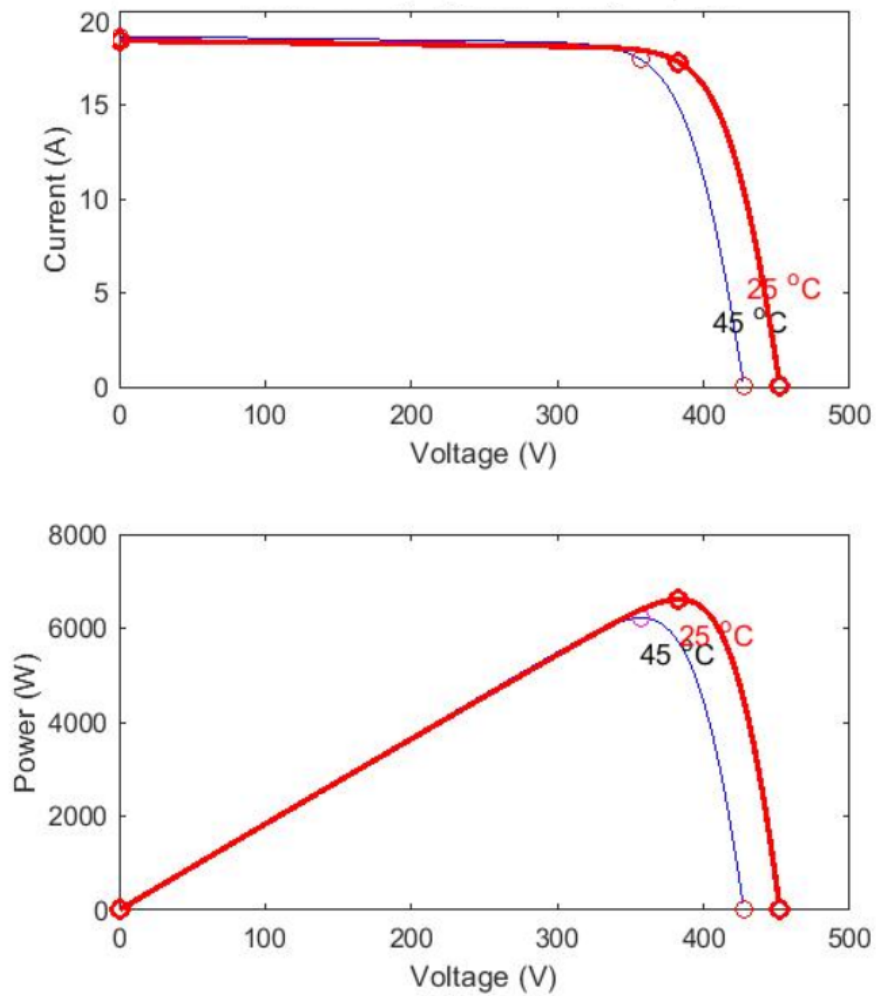


**Figure 3.10:** I-V and P-V characteristics of the PV array type: SunPower SPR-315E-WHT-D; 7 series modules; 3 parallel strings at 25° and 45°[1].

**Table 3.3:** Rated values of PV converter.

$L$	Inductance	5 mH
$C$	Capacitance	330 $\mu$ F
$r_c$	Equivalent series resistance	0.015 $\Omega$
$k_{pv}$	Proportional gain of P-controller	0.2
$V_{ref}$	Reference voltage at MPPT	380 V
$I_{pv}$	Constant current at MPPT	18 A

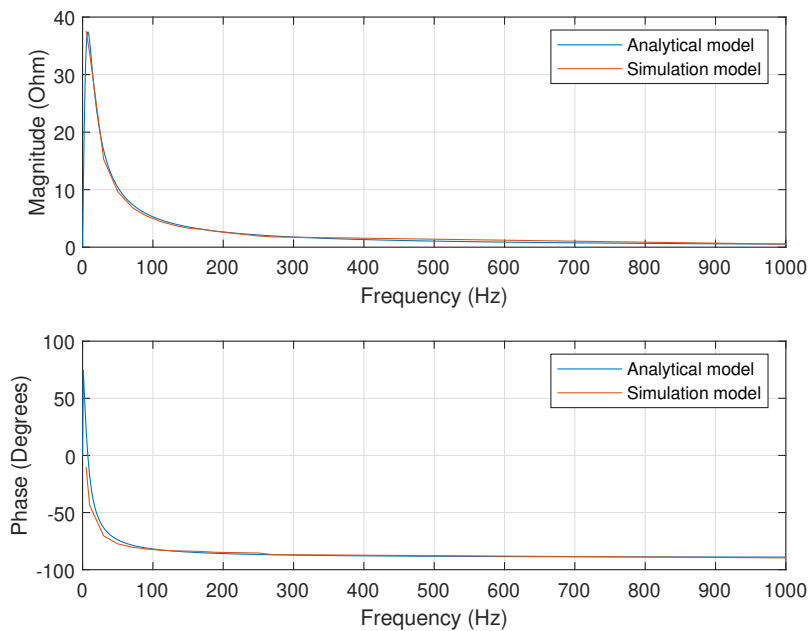


**Figure 3.11:** Impedance verification of PV system for analytical and simulation models.

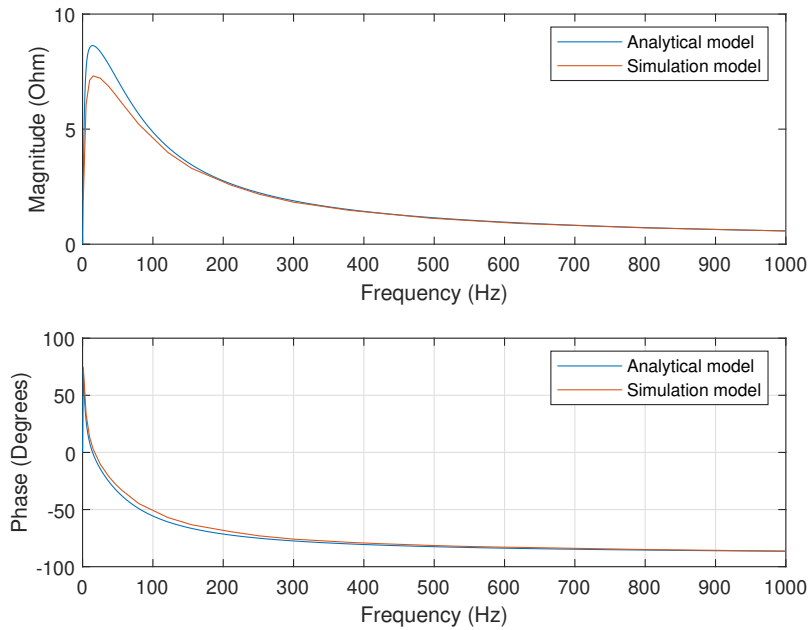
Figure 3.11 is the input impedance plot for the PV converter. It shows that both the simulation and mathematical model (derived in expression 3.1) match well for the overall frequency range. There is a deviation at a low frequency which can be attributed to the FFT calculation error in simulink, where it is difficult to extract the lower frequencies values.

### 3.3.3 Verification of Energy Storage Impedance Model

#### 3.3.3.1 Bidirectional Converter Working as Boost Converter

**Table 3.4:** Rated values of energy storage (discharging).

$L$	Inductance	50 mH
$C_1$	Input filter capacitance	15 $\mu$ F
$C_2$	Output filter capacitance	300 $\mu$ F
$r_l$	DCR of an inductor	0.02 $\Omega$
$r_c$	Equivalent resistance	0.002 $\Omega$
$k_{pv}$	Proportional gain of voltage controller	0.35
$k_{iv}$	Integral gain of voltage controller	5
$k_{pi}$	Proportional gain of current controller	0.01
$k_{ii}$	Integral gain of current controller	5



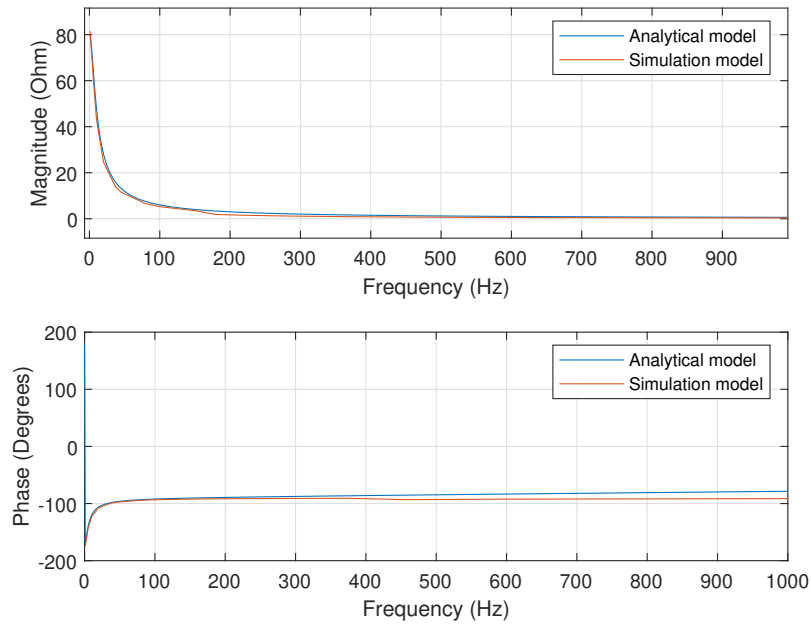
**Figure 3.12:** Impedance verification of energy storage discharging.

Figure 3.12 is the impedance plot for a bi-directional converter working in boost (discharging) mode. As can be observed from the plots, for the impedance in the magnitude part, there is a difference between them at the peak. But with an increasing frequency, the difference between the curves decrease and both follow each other. Similarly, curves for the phase plot also follow each other.

### 3.3.3.2 Bidirectional Converter Working as Buck Converter

**Table 3.5:** Rated values of energy storage (charging).

$L$	Inductance	50 mH
$C_1$	Input filter capacitance	15 mH
$C_2$	Output filter capacitance	300 $\mu$ F
$r_l$	DCR of an inductor	0.02 $\Omega$
$r_c$	Equivalent resistance	0.002 $\Omega$
$k_{pv}$	Proportional gain of voltage controller	30
$k_{iv}$	Integral gain of voltage controller	10
$k_{pi}$	Proportional gain of current controller	0.8
$k_{ii}$	Integral gain of current controller	0.1

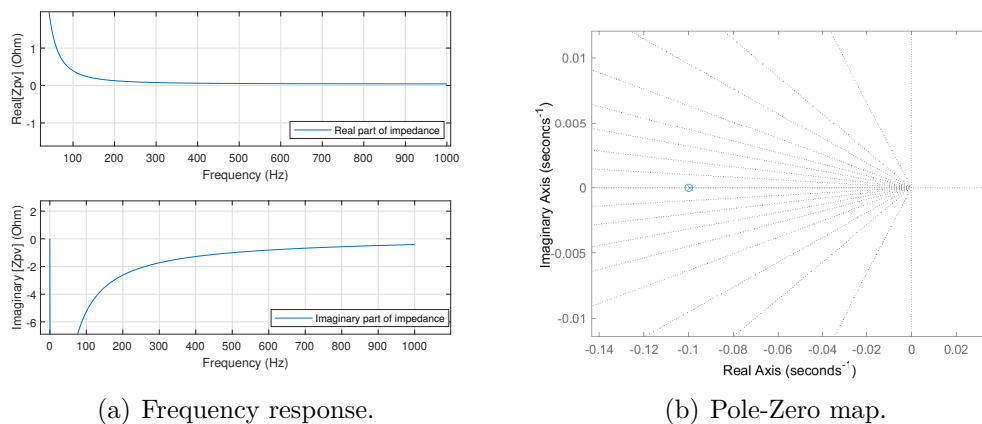


**Figure 3.13:** Impedance verification of energy storage - charging.

Figure 3.13 is the impedance plot of the bi-directional converter during charging (buck) mode. The magnitude of impedance decreases with increasing frequency and also the phase approaches  $-90^\circ$  and remain constant at higher frequencies. Both the analytical model (derived in 3.5) and simulation curves match good, indicating that the derived transfer function is a good approximation of the simulated model.

### 3.4 Passivity Analysis of Individual Systems

In this section the passivity of the individual converter models derived in previous chapter will be verified.



(a) Frequency response.

(b) Pole-Zero map.

**Figure 3.14:** Passivity plots for PV impedance model.

As shown in Figure 3.14(a) for the PV system, the plot of the real part of the impedance has resonance peak at the lower frequencies and approaches to zero as the frequency increases but never goes below zero. This assures that the real part of the impedance is non-negative for the entire frequency range. Moreover, as shown in Figure 3.14(b), the subsystem is stable as there are no poles on the right-half plane. Thus, according to the passivity definition, the PV system is taken as a passive system.

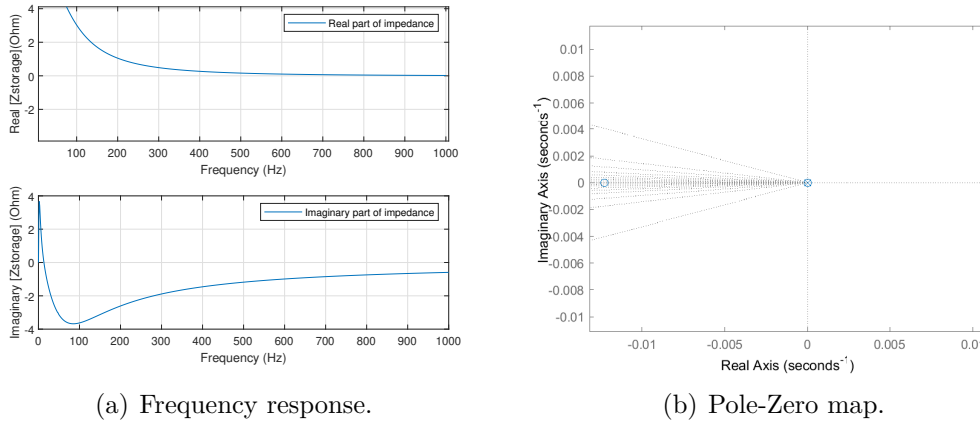


**Figure 3.15:** Passivity plots for energy storage impedance for charging.

Similarly, for the energy storage system, the plot for real part is positive for all frequencies and is stable as no poles on the right-half plane. Therefore, the system shows passive behavior. The frequency response plot and the pole-zero map are plotted in Figure 3.15(a) and 3.15(b) respectively.

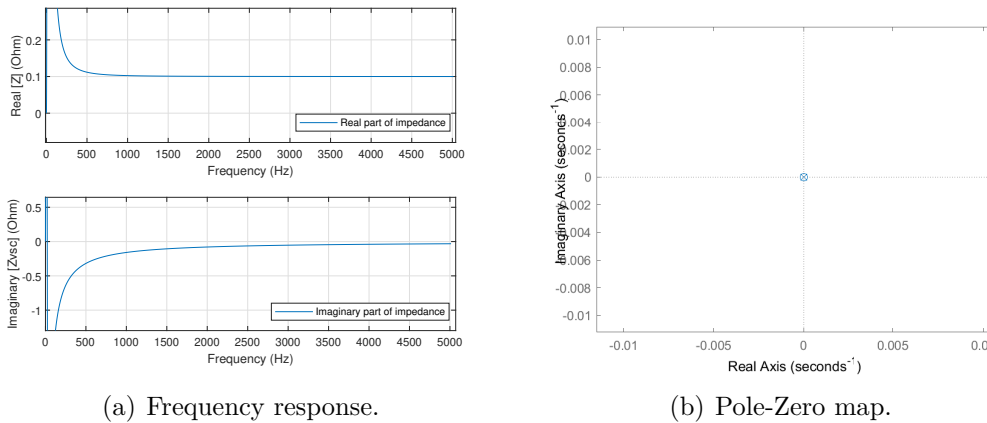


**Figure 3.16:** Passivity plots for VSC output impedance.

Figure 3.16(a) and 3.16(b) show the frequency response and pole-zero map of the VSC impedance model. The real part of the impedance is non-negative for the entire frequency range with a resonance peak at the lower frequencies and it is also stable from pole-zero map. This indicates that the VSC system is passive.

So far, the passivity of the subsystems from the VSC, energy storage and PV models has been verified, but for the CPL model, the real part of the admittance is non-negative and it does not fulfill the passivity theory. Thus, the CPL model could reduce the stability of the overall system.

### 3.5 Simplified Model of the System

In the dc-microgrid, impedance-based method is used for assessing stability of the system. It depends on the Middlebrook criterion which states that if two converters, one acting as a source converter and other as a load converter, are stable individually and output impedance of the source converter is less than the input impedance of the load converter in the entire frequency range, the stability of the cascaded system will be assured [18]. To apply this criterion in the Distributed Power System (DPS), the converters in the interconnected system have to be classified as a voltage source converter and current source converter based on the operating condition. In this paper, as grid-connected dc-microgrid is studied, the source converter at the dc-grid side acts as a VSC which regulates the dc-bus voltage. Therefore, its equivalent model is represented by a source voltage in series with the output impedance ( $Z_{vsc}$ ).

As the dc-bus voltage is already controlled by the VSC, the bi-directional converter on the energy storage and boost converter on the PV side can only affect the bus current by regulating their respective power. The PV converter controls its bus side current by regulating its input voltage using the MPPT control. The bi-directional converter also controls its bus side current by changing the charging current. Thus, the equivalent model for the PV converter, bi-directional converter and load converter is represented by a current source in parallel with input admittance to the converters at the point of connection ( $Y_{sub}$ ). The equivalent model for the impedance-based analysis is depicted in Figure 3.17. It shows a microgrid structure for the impedance-based analysis with one converter from each side.

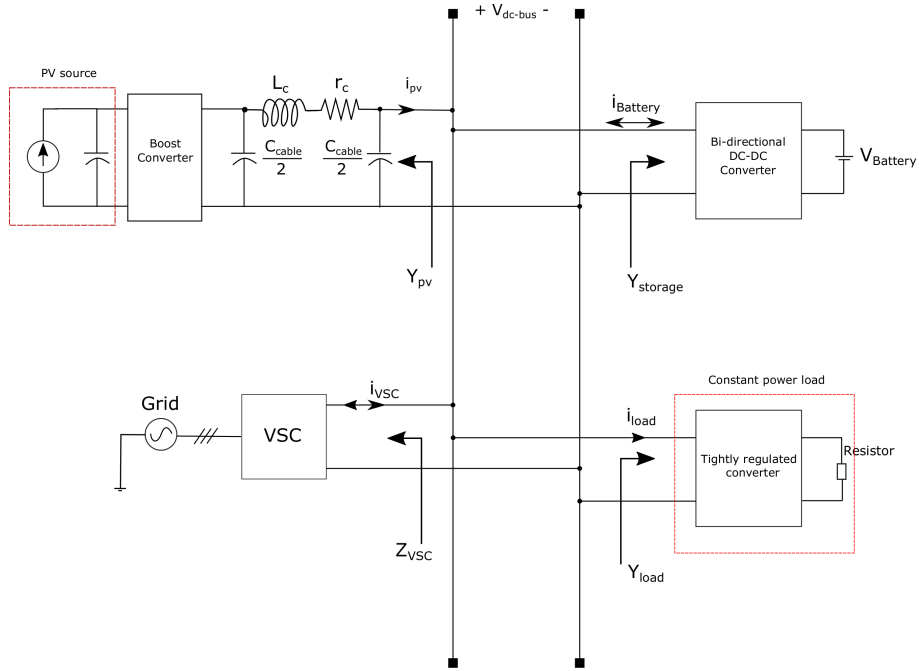


**Figure 3.17:** An equivalent model of the dc-microgrid for impedance based analysis.

With the system model in Figure 3.17, the overall system response is studied under different operating conditions. For simplifying the system analysis, the system is sub-divided into two components. On the source side, the VSC impedance,  $Z_{vsc}$  is taken as it acts as a voltage source and maintains the dc-bus voltage. The PV and energy storage are taken as current sources with their admittances  $Y_{pv}$  and  $Y_{storage}$  as they provide power by changing the current in the system. Similarly, the load is also represented as an admittance,  $Y_{load}$ .

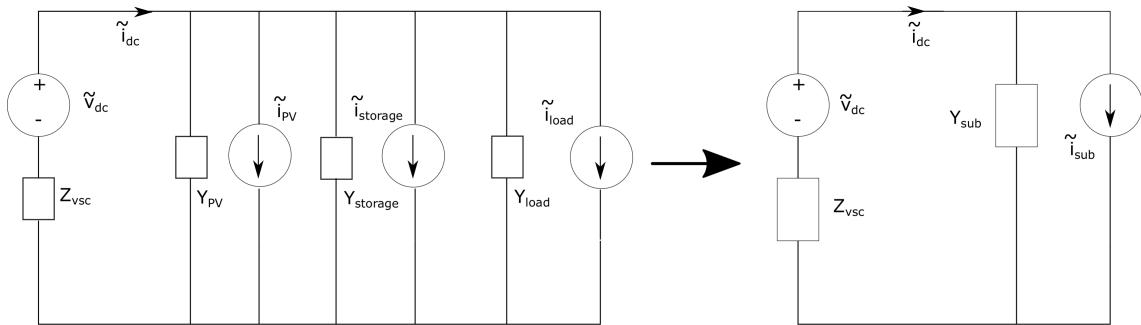


**Figure 3.18:** A simplified circuit of the dc-grid.

In Figure 3.18,  $Z_{vsc}$  is the impedance of the VSC connected in parallel to the common dc-bus.  $Y_{PV}$ ,  $Y_{storage}$  and  $Y_{load}$  are all connected in parallel to the dc-bus, their equivalent admittance is represented as  $Y_{sub}$ . From Figure 3.18, the equivalent dc-bus voltage can be obtained by applying superposition principle.

The voltage contribution from the voltage source,  $\tilde{v}_{vsc}$  is

$$\tilde{v}_1 = \frac{\tilde{v}_{vsc}}{1 + Y_{sub}Z_{vsc}}. \quad (3.7)$$

Similarly, for the current source,  $\tilde{I}_{sub}$  the voltage contribution is

$$\tilde{v}_2 = \frac{\tilde{I}_{sub}Z_{vsc}}{1 + Z_{vsc}Y_{sub}}. \quad (3.8)$$

Adding the two voltages (3.7), (3.8), the resultant dc bus voltage is

$$\tilde{v}_{dc} = \frac{\tilde{v}_{vsc} + \tilde{I}_{sub}Z_{vsc}}{1 + Z_{vsc}Y_{sub}}. \quad (3.9)$$

In (3.9),  $\frac{1}{1 + Z_{vsc}Y_{sub}}$  is the closed loop transfer function of the system with negative feedback. The forward path gain is 1 and the negative feedback gain is  $F(s) = Z_{vsc}Y_{sub}$ . The overall closed loop function is stable only if  $F(s)$  fulfills the Nyquist criteria i.e if there is no encirclement of  $(-1,0)$  and there should no be pole present in right side of the s-plane.

After studying the stability of the dc-microgrid with overall system, a capacitor bank will be connected across the dc-link capacitor and its effect on the stability of the system will also be studied. The capacitance of each capacitor in the bank is 7 mF (appendix A) and its circuit diagram is shown in Figure 3.19.

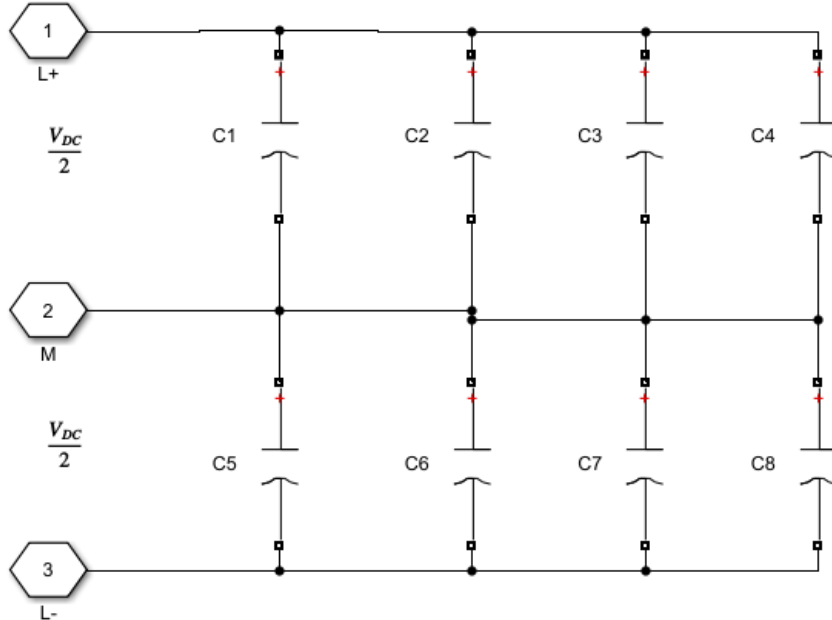


**Figure 3.19:** Circuit connection of the capacitor bank.

# 4

## Results and Analysis

In this chapter, the analytical results are validated with the simulation results. Several case scenarios have been taken to study stability issue in the dc-microgrid using the impedance-based method discussed in Chapter 2. In the first case scenario, the normal operation of the system is verified by taking a fixed load power and a fixed reference point for MPPT control. In the second scenario, the effect of load changes on stability is studied by increasing the load demand. The effect of the control parameters of the VSC on the system stability has been validated in the third scenario. The fourth scenario studies the impact of BESS on the overall system stability. The fifth and sixth scenarios are of adding a capacitor bank and implementation of a droop control in VSC and their impact on the overall stability of the system.

### 4.1 Case Scenario One: Normal Working Condition

In normal working condition, a CPL of 50 kW is connected to the dc-grid. The PV panel, which is producing power around 6.7 kW, is taken from two places of the building. Three converters are connected in parallel on each side of the building and overall around 40 kW power is generated from the PV panels. The remaining 10 kW comes from the VSC (28 kW rating) connected to the ac-grid and the power balance is satisfied. Moreover, the bandwidths for the controllers in the VSC are 10 Hz for the voltage and 100 Hz for the current controller respectively. The solar irradiance is  $1000 \text{ W/m}^2$  which corresponds to a maximum PV current of 54 A for our system with a PV string voltage of 380 V.

The analytical model, which is verified in Chapter 3, is applied to predict the stability of the system. The passivity of each subsystem is studied and all the subsystems except the load model are passive for most frequency range. Thus, the load could decrease the stability of the overall system and the Nyquist criterion can be used to study the stability of the system. From Figure 4.1(a), it can be observed that there is no encirclement of  $(-1,0)$ . Moreover, from Figure 4.1(b), no poles on the right side of the s-plane, hence by Nyquist analysis the system is stable.

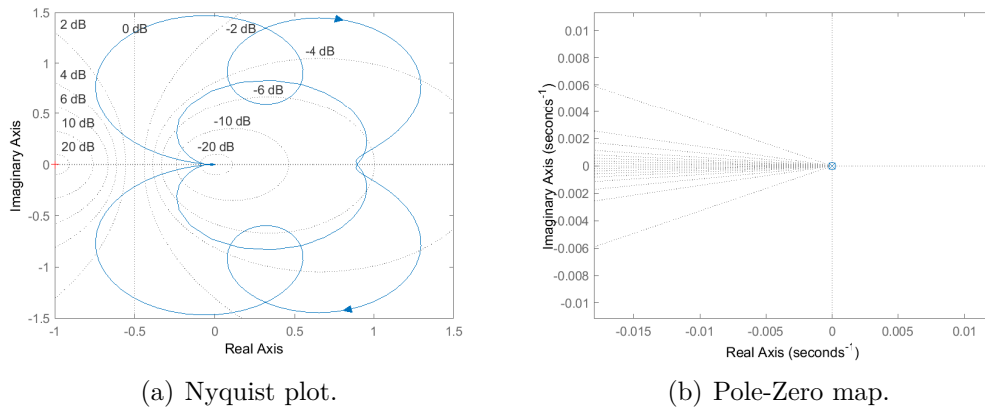


**Figure 4.1:** Nyquist and Pole-Zero plots of the open loop transfer function  $F(s)$  for normal working condition.

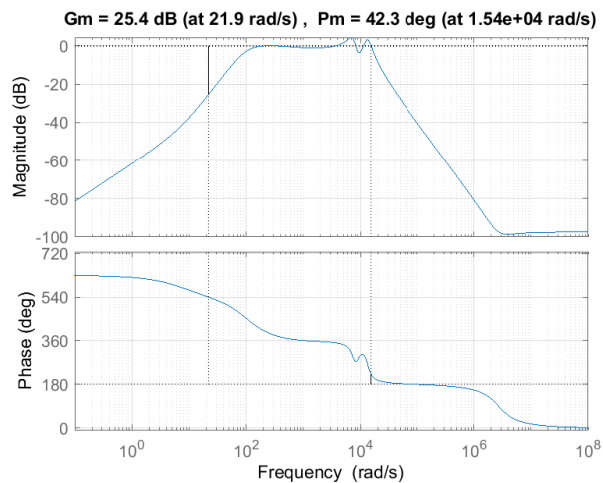


**Figure 4.2:** Gain and phase margins of open loop transfer function  $F(s)$  for the normal operating condition.

Since the overall system is stable as seen from the Nyquist analysis, however, to determine how close to instability the system is, the gain and phase margins of the system could be studied. A system that has a gain margin greater than one is stable, if any system has a gain margin less than one, it is unstable and the controller parameters must be adjusted to increase the gain. The phase margin of is recommended for good stability [7]. From the plot in Figure 4.2, both the phase and gain margins of the system are within the acceptable range indicating that the system is in a good stable condition.

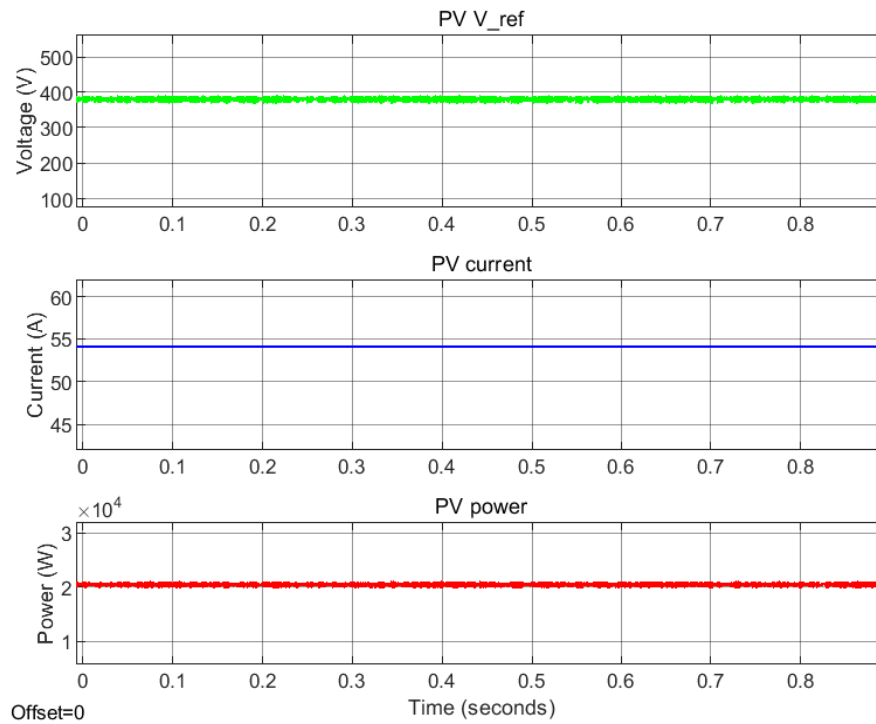


**Figure 4.3:** PV output plots for the grid connected system.

Figure 4.3 shows the simulation PV output plots for the grid-connected DC microgrid, i.e at the AWL building. In the analytical model, there are a total of six PV converters each with a power production around 6.7 kW, three in each AWL and SB3 building. In the simulation model, however, the three converters in one building are scaled using per unit, and resulting there are two PV boost converters each with an effective power production around 20 kW. For each of these two converters, the reference voltage for the MPPT controller is set at 380 V and a current source is taken to imitate the current from the PV panel, rated value is taken as 54 A (18x3), 18 A being the current generated by each PV panel.

From Figure 4.3 it can be observed that the reference voltage is at 380 V, the generated current is 54 A, and output power is 20 kW at steady state. Similar waveforms can be observed for the converter at SB3 as well. The resulting output power from the two converter systems together is 40 kW, which is provided to the load.

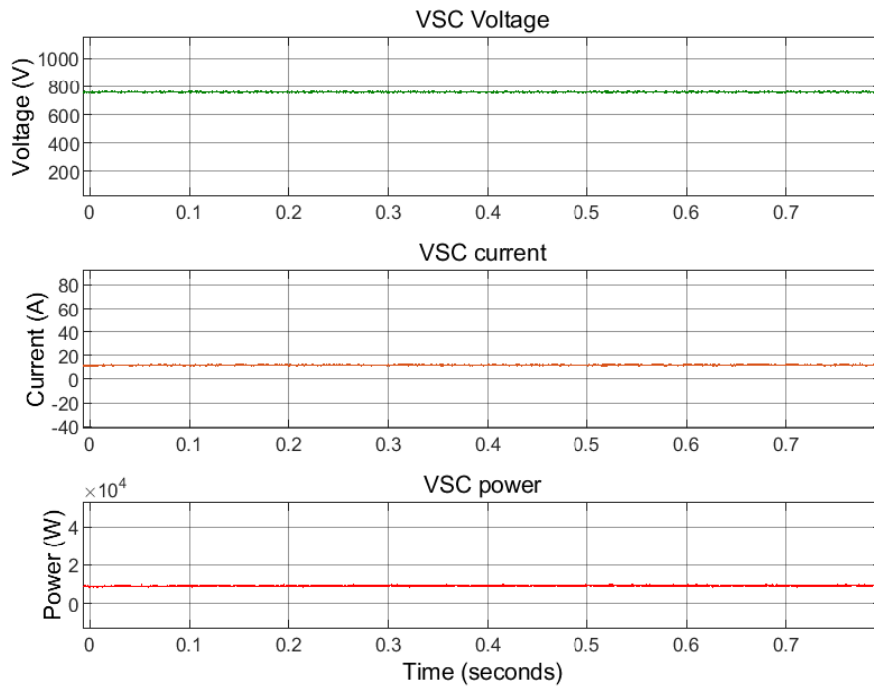


**Figure 4.4:** Grid connected VSC output plots.

Figure 4.4 is the plot for output voltage, current, and power of the grid connected VSC. The simulated system is stable as it maintains the bus voltage at 760 Vdc. For the load of 50 kW, as 40 kW is provided by the PV, the remaining 10 kW power comes from the ac-grid which can be observed from the plot.

## 4.2 Case Scenario Two: Effect of Increasing Load

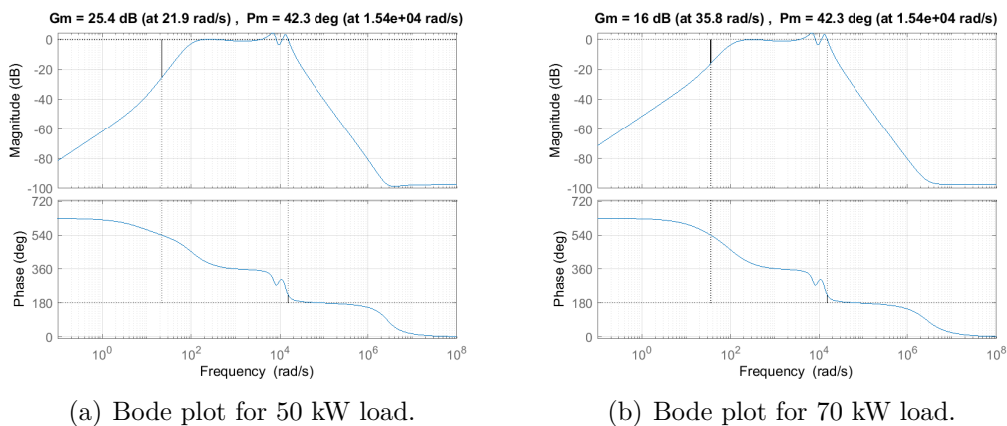


**Figure 4.5:** Bode plot comparison for increasing load from 50 kW to 70 kW.

In this scenario, the load is increased from 50 kW to 70 kW to study its effect on the system stability. Since, the CPL characteristic is inherently non-passive in nature,

increasing the load further makes it less passive and it affects the stability of the overall system which is reflected in the bode diagrams. Figure 4.5(b) is the bode plot for the system described in scenario 4.1, but with a load of 70 kW. Compared to Figure 4.5(a) with a gain margin of 25.4 dB it can be observed that it has reduced significantly to 16 dB whereas phase margin remains unchanged as the CPL model has a resistive behavior. This can be attributed to the increased CPL which affects the gain margin of a system.

Figure 4.6 is the simulated bus voltage output for the system with an initial load of 50 kW and adding a load step of 20 kW at 0.2 s. The system is stable with both load values. This indicates that the system is less affected by a small increase in the resistance from the load side. However, for determining the relative stability, the bode plot analysis can be used.

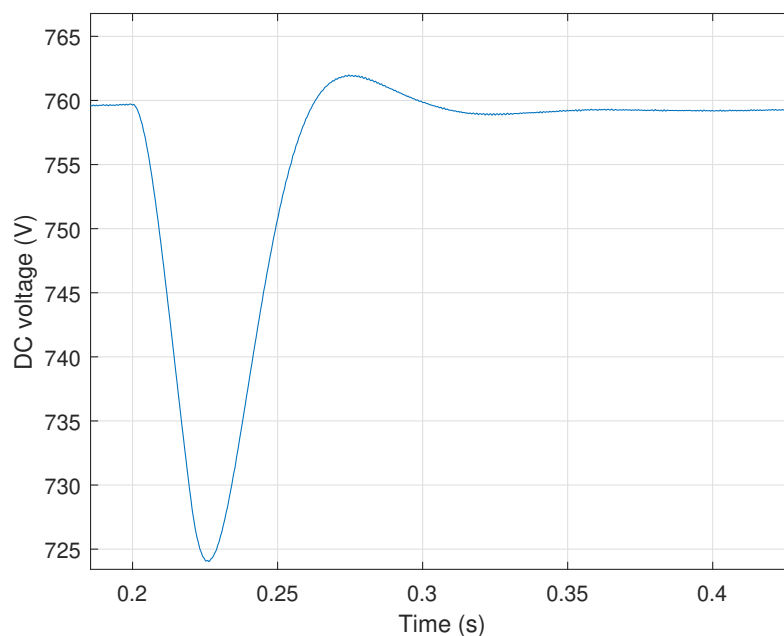


**Figure 4.6:** DC bus voltage for a 20 kW load step from 50 kW to 70 kW at 0.2 s.

### 4.3 Case Scenario Three: Effect of Increasing Controller Bandwidth

In this case study, the bandwidths of the voltage and current controller of the VSC will be increased to study the impact on stability of the system. For voltage controller, the bandwidth is increased from 10 Hz, 20 Hz to 30 Hz. Similarly, for the current controller, bandwidth is increased from 100 Hz, 200 Hz to 300 Hz. The bandwidths are so chosen to ensure that the current controller is 10 times faster than the voltage controller.

### 4.3.1 Increasing VSC Voltage Controller Bandwidth

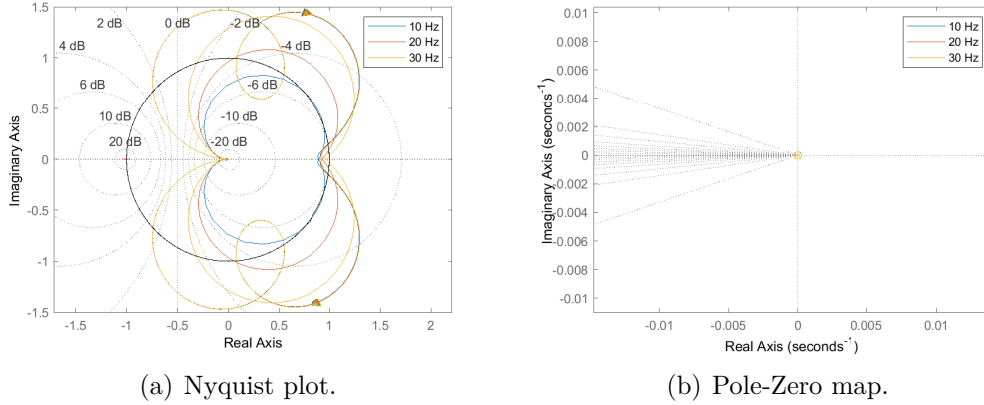


**Figure 4.7:** Nyquist and Pole-Zero map of open loop transfer function  $F(s)$  for increasing VSC voltage controller bandwidths of 10 Hz, 20 Hz and 30 Hz.

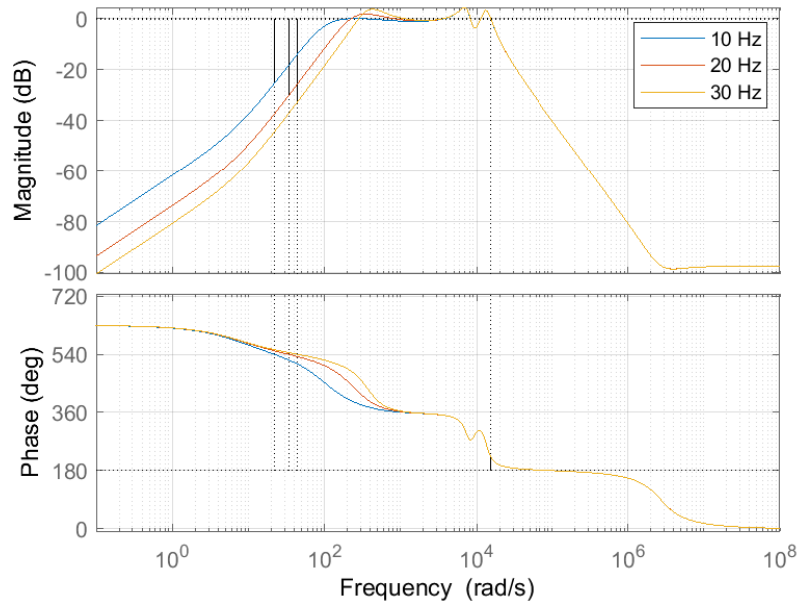


**Figure 4.8:** Bode plots of open loop transfer function  $F(s)$  for increasing voltage controller bandwidths of 10 Hz, 20 Hz and 30 Hz.

The voltage controller bandwidth of the VSC is gradually increased while keeping the current controller constant at 100 Hz to study the effect on the system stability. As observed from the Nyquist and pole-zero plots in Figure 4.7(a)-4.7(b), the system is stable for all three bandwidths 10 Hz, 20 Hz and 30 Hz. However, to compare the relative stabilities at the three frequencies, bode plot analysis is required. From Figure 4.8 it can be observed that as bandwidth is increased, the gain margin increases

with maximum gain margin of 32.5 dB at 30 Hz voltage controller bandwidth, making the overall system relatively more stable. The phase margin remains the same at 42.3deg, this can also be seen in the Nyquist plot 4.7(a), where in the outer loop all the three curves overlap each other, as such they all have the same intersection point for the unit circle taken with center (0,0). Increasing voltage controller bandwidth for the VSC affects the input impedance of the model and it can be explained from passivity theory. Figure 4.9 shows the frequency response of the VSC for the three different bandwidths. The impedance model still shows the passivity behavior, but the resonance peak for the impedance decreases as the voltage-controller bandwidth increase. According the Middlebrook criterion, as explained in Section 3.5, the input impedance of the source converter should be less than the input impedance of the current converter for the interconnected system to be stable. In this study, the VSC is acting as the source converter that regulates the dc-bus voltage and the impedance decreases with increasing the voltage bandwidth. Thus, the overall stability will be improved.

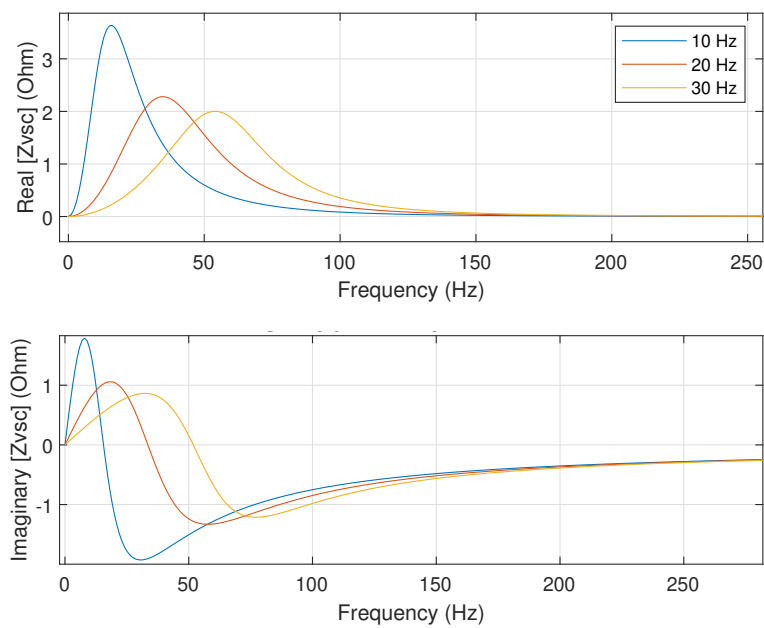


**Figure 4.9:** Frequency response of VSC for increasing voltage controller bandwidth from 10 Hz, 20 Hz to 20 Hz.

### 4.3.2 Increasing VSC Current Controller Bandwidth

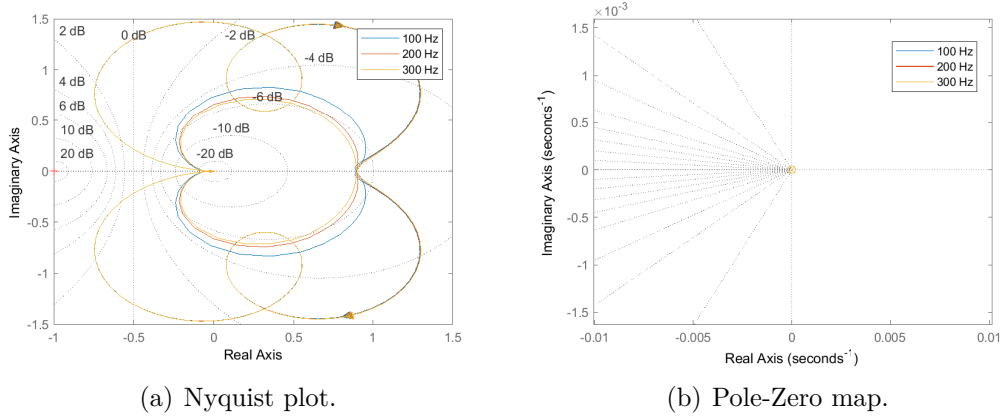


**Figure 4.10:** Nyquist and Pole-Zero map of open loop transfer function  $F(s)$  for increasing VSC current controller bandwidths of 100 Hz, 200 Hz and 300 Hz.

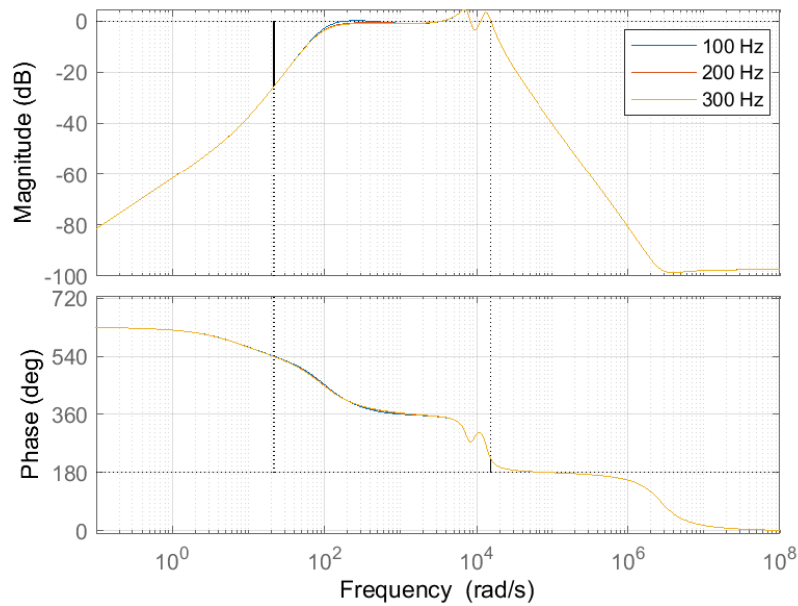


**Figure 4.11:** Bode plots of open loop transfer function  $F(s)$  for increasing VSC current controller bandwidth of 100 Hz, 200 Hz and 300 Hz.

In this scenario, the bandwidth of the current controller in VSC is gradually increased keeping the voltage controller fixed. Figures 4.10(a), 4.10(b) are the Nyquist and pole-zero map for the system. As observed from both the plots, the system is stable for all three bandwidths 100 Hz, 200 Hz and 300 Hz of the current controller as there is no encirclement of  $(-1,0)$  on the Nyquist plot and also no poles present on the right-half side of the s-plane. Figure 4.11 shows the bode plots for the increasing

current controller bandwidths. It can be observed that the gain margin increases slightly from 25.4 dB to 26 dB with bandwidth increase from 100 Hz-300 Hz, however, compared to the case where voltage controller bandwidth is increased, the increment in the gain margin is small, suggesting that current controller bandwidth effect is small. Phase margin however remains the same in the three cases. Passivity theory wise, increasing the current controller bandwidth does not affect the passivity of the VSC significantly which could affect the overall system stability. This can be observed from the frequency response plots for increasing current controller bandwidths in Figure 4.12, where the change in real and imaginary part of the impedance is small for increasing current controller bandwidths.

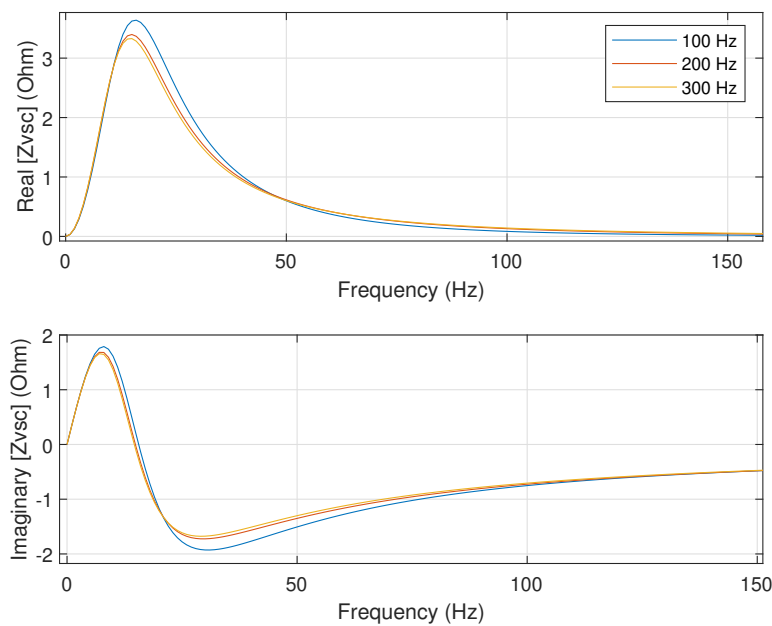


**Figure 4.12:** Frequency response of VSC for increasing current controller bandwidths.

#### 4.4 Case Scenario Four: Effect of Adding Energy Storage

In this scenario, the effect of adding a battery storage system is studied. A 6 kW BESS is added to the system, its effect on the overall system stability for both charging and discharging cycles is studied. In the charging mode, the VSC maintains the dc-bus voltage and the solar panels provide power to the load and also to charge the battery. In the discharging state, the VSC is disconnected, as such the energy storage needs to maintain the dc-bus voltage level until power from the grid is restored. These two modes of operation will be studied in the next subsection.

### 4.4.1 Charging Mode

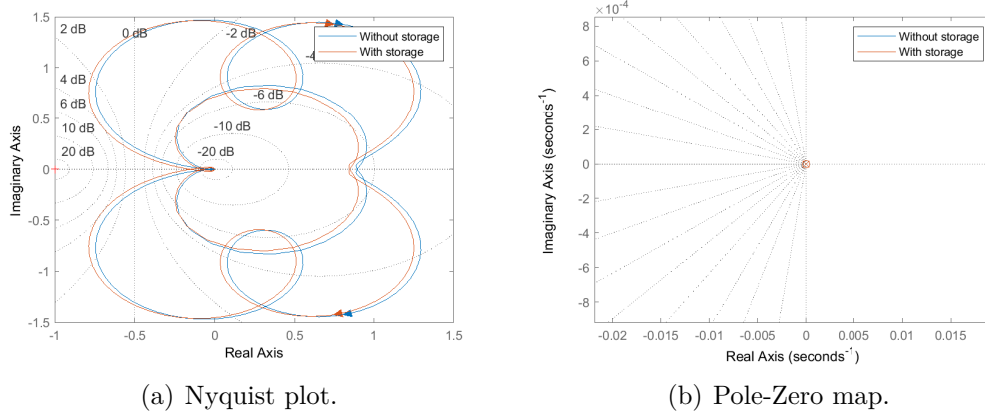


**Figure 4.13:** Nyquist and Pole-Zero map of open loop transfer function  $F(s)$  with and without energy storage during charging.

For the charging mode operation, the Nyquist and pole-zero map for the analytical model is studied and the result is analyzed with the time-domain simulation. Figure 4.13(a) and 4.13(b) are the Nyquist and pole-zero map for the system with and without the energy storage during charging mode. It can be observed that the system is stable with the energy storage added.

To investigate the effect of the BESS on the stability of the system, the gain and phase margins could be observed before and after the energy storage is added. Figure 4.14(b) is the bode plot for the BESS in charging mode. Comparing to the first case with only the PV, ac-grid, and load as in Figure 4.14(a) it can be seen that the gain margin as well as the phase margins decrease. This is due to the energy storage in charging mode which acts as an additional load, reducing the system stability.

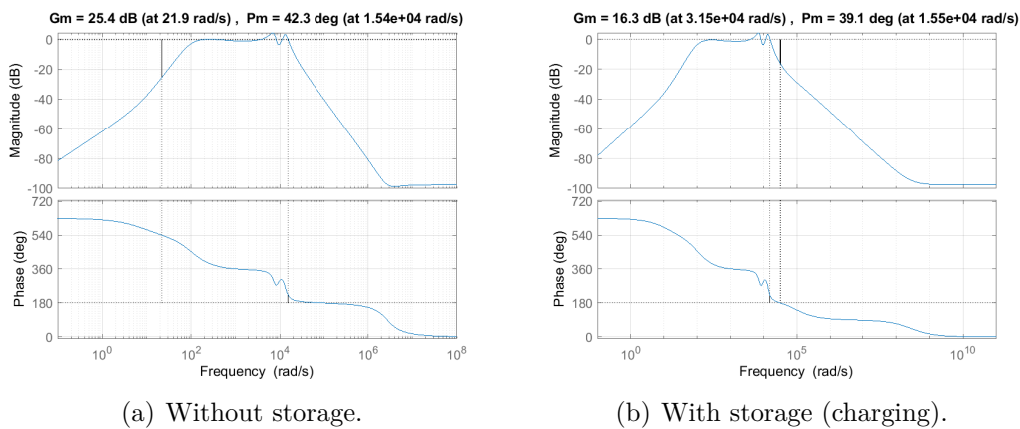


**Figure 4.14:** Bode plot of open loop transfer function  $F(s)$  for energy storage model in charging mode.

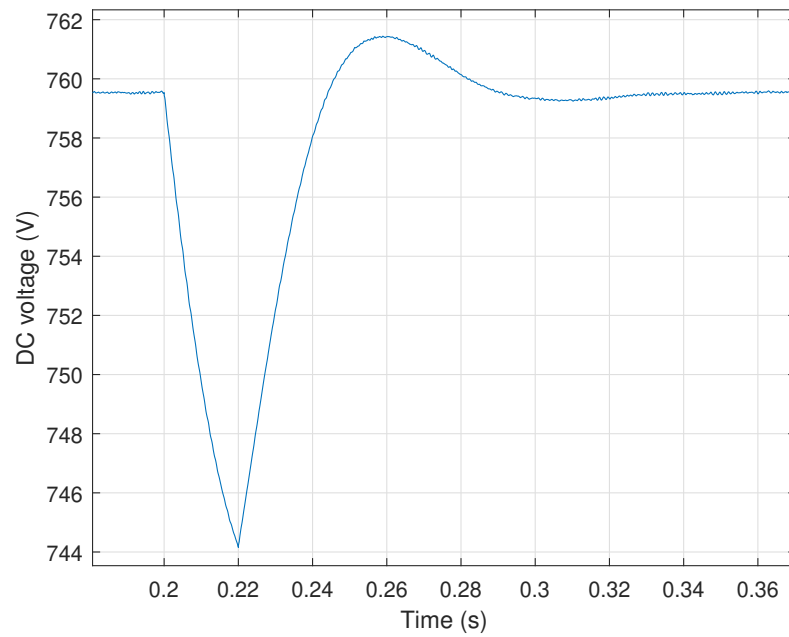


**Figure 4.15:** DC bus voltage during charging mode with an energy storage added at 0.2 s.

Figure 4.15 is the dc bus voltage with time-domain stimulation when the BESS is added. The output voltage is 760 V at a steady-state indicating a stable system.

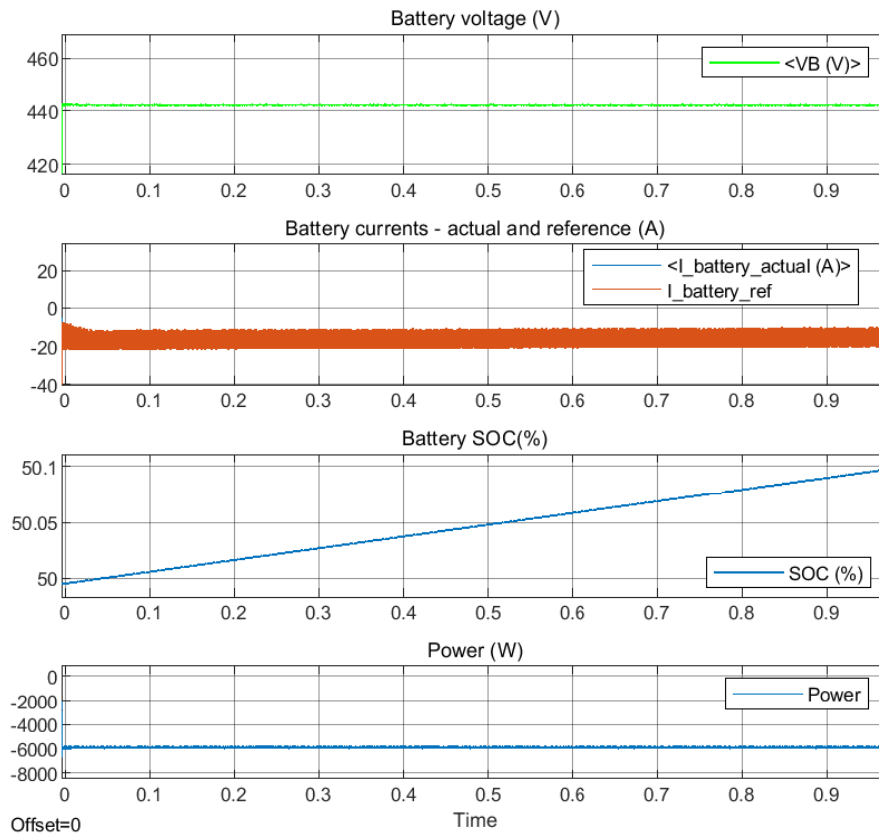


**Figure 4.16:** Charging wave forms for the energy storage.

Figure 4.16 gives the simulation battery voltage, current, and SOC during charging mode. The BESS power is 6 kW with a nominal battery voltage of 380 V and the battery could charge to a maximum voltage of 442 V. This data is taken from the battery block selected from the Simulink library. It can be observed from the figure that the battery voltage is maintained at 442 V and the charging current is around  $-20$  A (negative indicates charging mode), the initial SOC level of the battery is assumed to be 50% and it keeps increasing with time.

#### 4.4.2 Discharging (Islanded) Mode

When the ac-grid is disconnected from the system due to a fault, the dc-microgrid should work in islanded mode for some time depending on the capacity of the energy storage. The energy storage regulates the dc-bus voltage and at the same time provides power to the load if the power demand can not be covered by the PV.

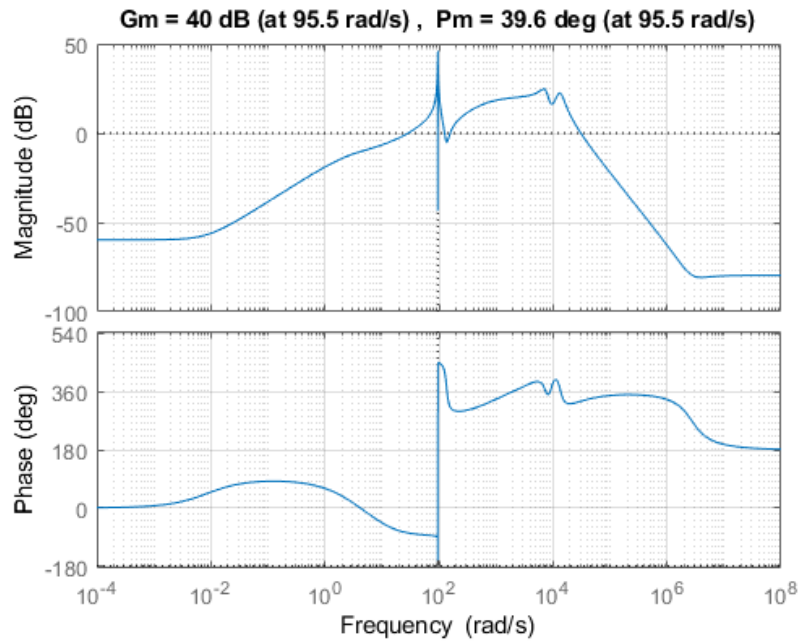


Figure 4.17: Bode plot for the the energy storage model during discharge.

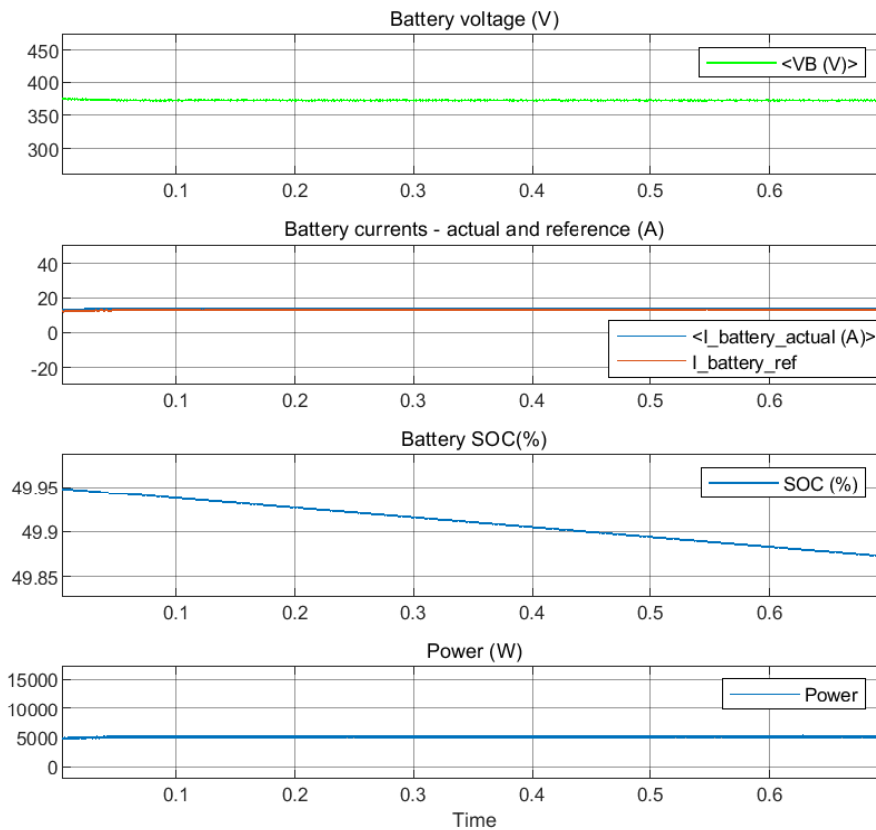


Figure 4.18: Discharge waveform for the energy storage.

As shown in Figure 4.18, the battery is maintaining its voltage around the nominal

value 380 V in steady state. The reference current for the inner current controller is determined by the outer voltage controller and the actual current is tracking the reference current. It is also seen that the SOC is decreasing from its initial value. In the islanded mode, the PV side is generating its maximum power at the previously specified reference voltage when it was working in grid-connected mode. Since the load is 50 kW, the PV can supply a max of 40 kW, the remaining is provided by the BESS.

## 4.5 Case Scenario Five: Effect of Adding a Capacitor Bank

In this scenario, the effect of adding a capacitor bank on the stability of the overall system is studied. From the dc-link in the real system, capacitor value is replaced with the equivalent one with each capacitance of 7 mF. To determine the overall stability of the system Nyquist and pole-zero map is plotted in Figure 4.19(a) and 4.19(b). It is observed that adding a capacitor bank improves the stability of the system.

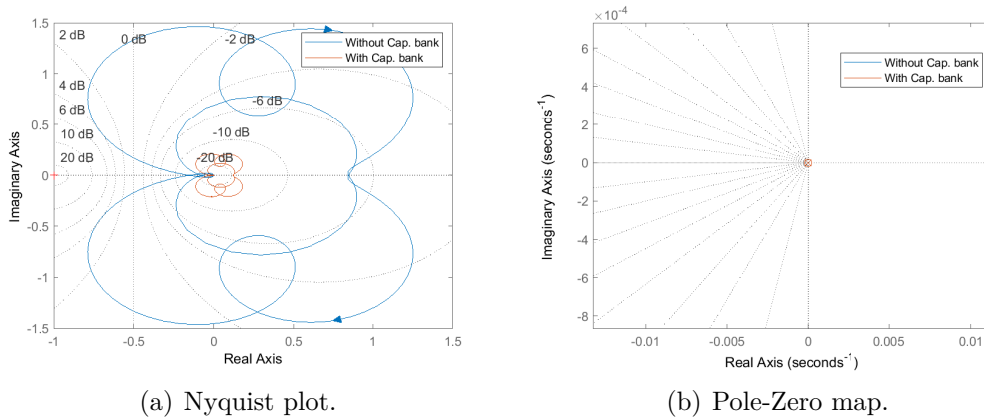


**Figure 4.19:** Nyquist and Pole-zero map of open loop transfer function  $F(s)$  with and without a capacitor bank.

Since the capacitor bank changes the capacitance value of the dc-link capacitor, the input impedance of the VSC also changes. The frequency response of the input impedance for the VSC model has been depicted in Figure 4.20 to check its passivity when the capacitor bank is connected. It can be observed from the plot that increasing the capacitance of the dc-link capacitor reduces the resonance peak that occurs at some frequencies. This is useful for the impedance ratio to be less than one and this leads the stability of the overall system to be guaranteed.

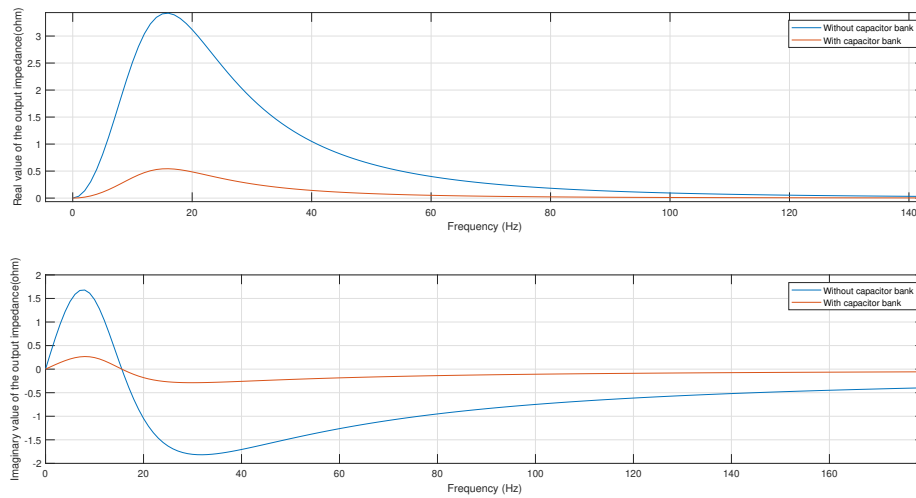


**Figure 4.20:** Frequency response of the VSC after adding a capacitor bank.

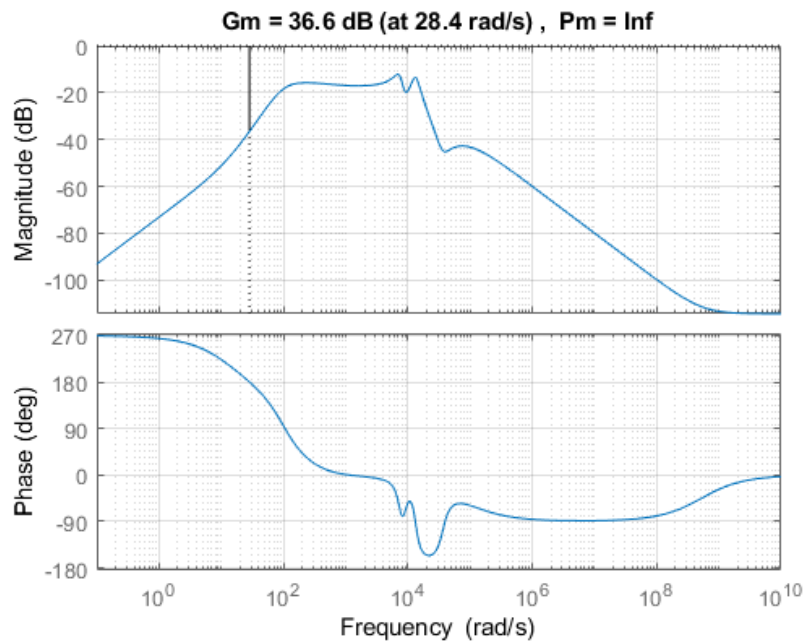


**Figure 4.21:** Bode plot of open loop transfer function  $F(s)$  with a capacitor bank added to the system.

For further analysis, the bode diagram of the system is plotted in Figure 4.21. It shows that the gain is always below zero for all frequency range and the phase margin becomes infinite. Moreover, the gain margin increases from 25.4 dB (without the capacitor bank) to 36.6 dB. Having a gain or phase margins of extremely large value slows down the response of the system and gets a problem in tracking the reference. The analytical result is verified with simulation as shown in Figure 4.22 which shows that with a capacitor bank added, the system is not easily affected by

disturbances.

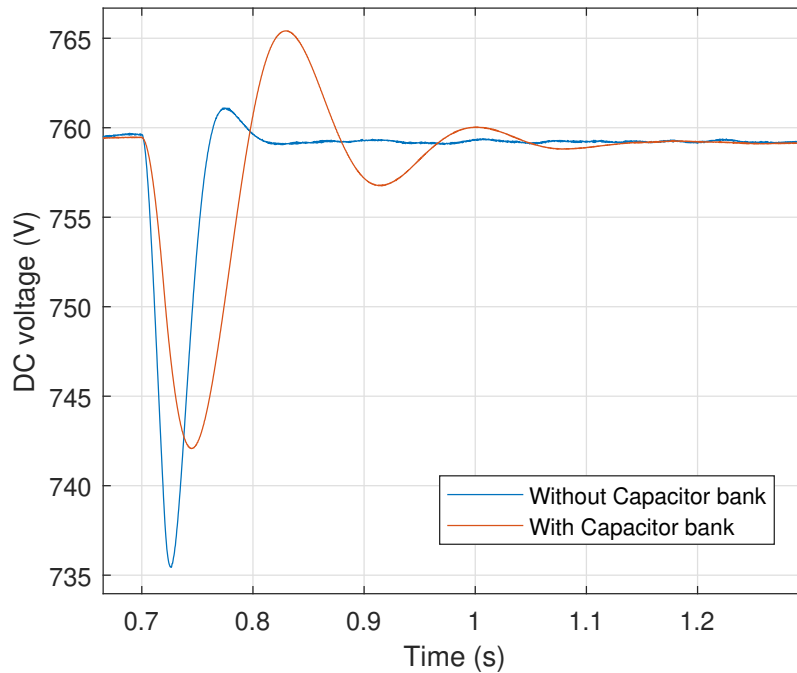


**Figure 4.22:** DC-bus voltage with and without a capacitor bank for a load step of 20 kW at 0.7 s.

## 4.6 Case Scenario Six: Effect of Adding a Droop Control

In this scenario, the droop in the VSC is increased gradually to study the effect on system stability. Figure 4.23(a) and 4.23(b) are the Nyquist and pole-zero plots for the overall system with an increasing droop term. As there are no poles on the right hand plane in the the pole-zero map and no  $(-1,0)$  encirclements in the Nyquist plot for any of the droop values, the overall system is stable for all the three cases. However, to analyze the relative system stability for the different droop coefficients, bode plot analysis is performed in the next section.

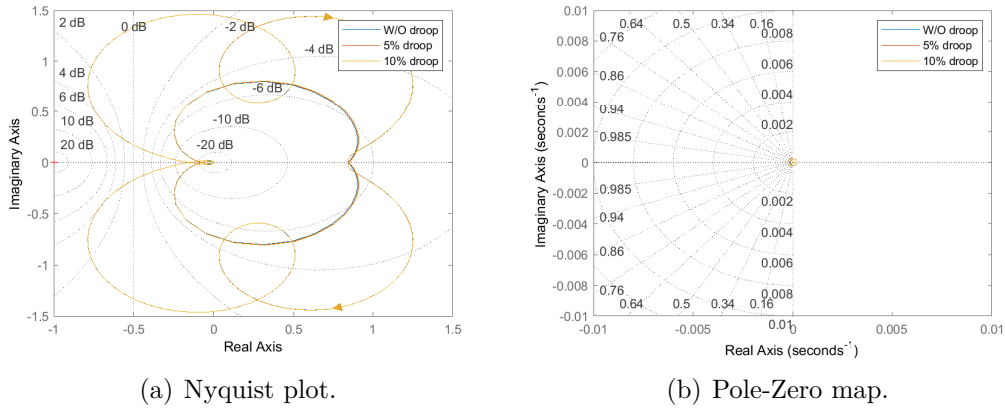


**Figure 4.23:** Nyquist and Pole-Zero map of open loop transfer function  $F(s)$  for increasing droop.

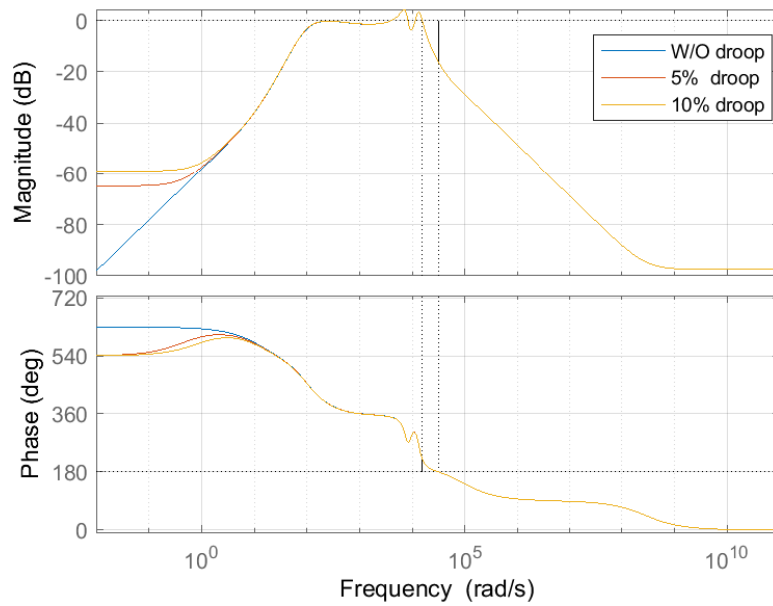


**Figure 4.24:** Bode plots for increasing droop of VSC starting with no droop, 5% droop and 10% droop.

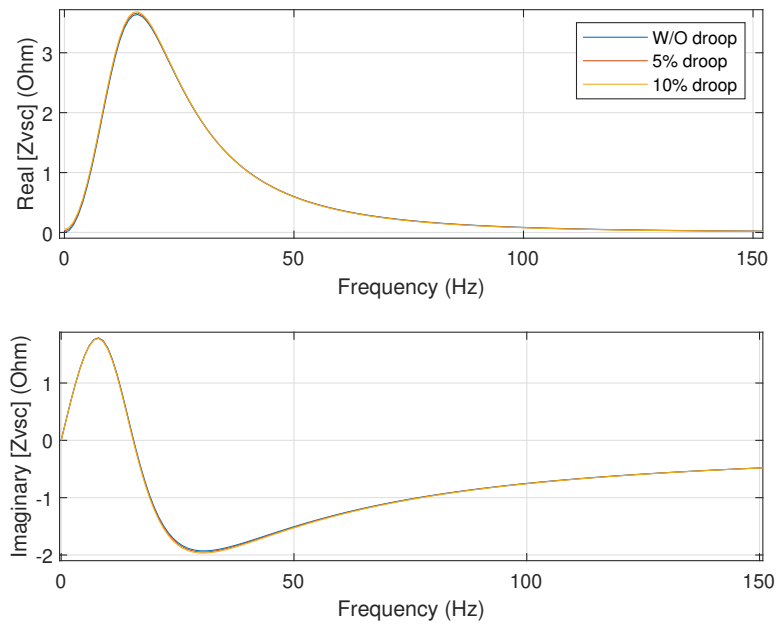


**Figure 4.25:** Frequency response of VSC for increasing droop gain.

As seen from the bode plot in Figure 4.24, with an increasing droop the phase margin decreases very little from 39.1 deg to 39 deg while the gain margin remains the same at 16.3 dB, which implies that the system isn't affected much by change in the droop parameter. This can be explained from the frequency response plot of the VSC in Figure 4.25 where the VSC impedance doesn't have much change for increasing droop to 5% and 10%.

# 5

## Sustainability

### 5.1 Sustainability Aspects

Sustainable development aims for human welfare without adversely affecting other associated factors. These factors can be classified into three types, they are ecological, economical and social factors. Each of these factors will be discussed from the perspective of our work in the following subsections.

#### 5.1.1 Ecological Aspect

The dc-microgrid has a large number of solar panel installations. As the panels are mounted on the roof, no extra land space is required. Moreover, since they are operated in a colder climate, the panels have higher efficiency [19] and is a clean energy source with no emissions. Furthermore, the use of solar optimizers ensures that maximum power is obtained which is also environmentally beneficial.

One environmental disadvantage could be the battery storage pack used in our system. Since lithium-ion batteries are used, proper handling of the batteries at the end of life can be a challenge.

#### 5.1.2 Economical Aspect

An initial investment in setting up the PV system could be high, but since these panels have a long life, they make up for the cost over time. Also, the dc-system requires less wire thickness for power transmission compared to ac systems, thereby cutting on cost.

#### 5.1.3 Social aspect

Society encourages the use of renewable and clean energy sources to reduce emissions and tackle climate change. As such people, in general would prefer to install solar panels to save on energy bills which would also benefit the environment.



# 6

## Conclusion and Future Work

### 6.1 Conclusion

The master thesis investigated the impact of power converters in a dc-microgrid. Initially, transfer functions were derived for each of the different converters used in the study. These transfer functions were then verified by comparing their impedance response with that of the simulation models. Combining all the derived transfer functions to form an overall system, the various case studies were carried out both analytically and with the simulation model.

In the first scenario the PV, load and VSC connected to the grid are taken to be operating together and the system was found to be stable both analytically and in simulation. In the second scenario, the load was increased by 40% from 50 to 70 kW. Since, the CPL is non-passive in nature, increasing the load only makes the system further less passive, decreasing the overall system stability. In the third scenario, the bandwidths of both the voltage and current controllers of the VSC were increased to observe any effect on stability. For the voltage controller bandwidth increase, the system was found to be more stable; this is due to the decrease in input impedance of the VSC. In the current controller bandwidth increase scenario, there is very little effect on the system passivity due to the negligible impact on the impedance of the VSC and there is no delay in the current controller. In the fourth scenario, a 6 kW Battery Energy Storage System (BESS) is added to the dc-grid and the system is studied for both charging and discharging mode of operation. In the charging scenario, the gain and phase margins decrease reducing the system stability as during the charging process, the BESS acts as an additional load connected to the dc-grid. For the discharging case, working in islanded mode, the storage system maintains the dc-bus voltage and the system is stable. In the fifth scenario, a capacitor bank with eight capacitors of 7 mF each is connected in series and parallel configuration. It is observed that adding the capacitor bank makes the overall system more stable as the input impedance of the VSC is reduced. However, this results in high gain and phase margin values which slows down the system response. In the sixth scenario, increasing the droop term of the VSC it is observed that the system's stability remains unaffected for a 5% or 10% increase. This is explained from the impedance plot of the VSC, where it can be observed a very minimal change for the increase of droop.

## 6.2 Future Work

For modelling the VSC, a suggested improvement could be to implement a Modular Multi-Level Converter (MMC) instead of a two-level converter. Furthermore, the effect of VSC cable length can be taken into consideration. The analytical converter transfer functions were verified with simulation models, for the future studies this verification can be done with real power converters. Additionally, another interesting future work can be to implement the test cases of the VSC voltage and current controller bandwidth change in the real system.

# Bibliography

- [1] Mathworks. (2020) Implement PV array modules. [Online]. Available: <https://se.mathworks.com/help/phymod/sps/powersys/ref/pvarray.html>
- [2] Nexans.se. (2020) 15152998. [Online]. Available: [https://www.nexans.se/eservice/Sweden-en/pdf-product\\_540327046/AXQJ\\_1\\_kV\\_3X240\\_72.pdf](https://www.nexans.se/eservice/Sweden-en/pdf-product_540327046/AXQJ_1_kV_3X240_72.pdf)
- [3] Nexans. (2020) 15153898. [Online]. Available: [https://www.nexans.se/eservice/Sweden-en/pdf-product\\_540352809/AXQJ\\_1\\_kV\\_4X50\\_16.pdf](https://www.nexans.se/eservice/Sweden-en/pdf-product_540352809/AXQJ_1_kV_4X50_16.pdf)
- [4] B. Hartono, R. Setiabudy *et al.*, “Review of microgrid technology,” in *2013 international conference on QiR*. IEEE, 2013, pp. 127–132.
- [5] J. Lee, B. Han, and N. Choi, “Dc micro-grid operational analysis with detailed simulation model for distributed generation,” in *2010 IEEE Energy Conversion Congress and Exposition*. IEEE, 2010, pp. 3153–3160.
- [6] A. Kwasinski and C. N. Onwuchekwa, “Dynamic behavior and stabilization of dc microgrids with instantaneous constant-power loads,” *IEEE Transactions on power electronics*, vol. 26, no. 3, pp. 822–834, 2010.
- [7] A. A. A. Radwan and Y. A.-R. I. Mohamed, “Linear active stabilization of converter-dominated dc microgrids,” *IEEE Transactions on Smart Grid*, vol. 3, no. 1, pp. 203–216, 2011.
- [8] Q. Peng, Q. Jiang, Y. Yang, T. Liu, H. Wang, and F. Blaabjerg, “On the stability of power electronics-dominated systems: Challenges and potential solutions,” *IEEE Transactions on Industry Applications*, vol. 55, no. 6, pp. 7657–7670, 2019.
- [9] G. Pinares and M. Bongiorno, “Analysis and mitigation of instabilities originated from dc-side resonances in vsc-hvdc systems,” *IEEE Transactions on Industry Applications*, vol. 52, no. 4, pp. 2807–2815, 2016.
- [10] M. K. AL-Nussairi, R. Bayindir, S. Padmanaban, L. Mihet-Popa, and P. Siano, “Constant power loads (cpl) with microgrids: Problem definition, stability analysis and compensation techniques,” *Energies*, vol. 10, no. 10, p. 1656, 2017.
- [11] H. Patel and V. Agarwal, “Maximum power point tracking scheme for pv systems operating under partially shaded conditions,” *IEEE transactions on industrial electronics*, vol. 55, no. 4, pp. 1689–1698, 2008.
- [12] X. Lu, K. Sun, J. M. Guerrero, J. C. Vasquez, L. Huang, and J. Wang, “Stability

- enhancement based on virtual impedance for dc microgrids with constant power loads,” *IEEE Transactions on Smart Grid*, vol. 6, no. 6, pp. 2770–2783, 2015.
- [13] S. J. Mason, “Feedback theory-further properties of signal flow graphs,” *Proceedings of the IRE*, vol. 44, no. 7, pp. 920–926, 1956.
- [14] W. Wu, A. Luo, Y. Chen, Y. Dong, L. Zhou, X. Zhou, L. Yang, Z. He, Q. Xu, and X. Huang, “Dc impedance modeling, stability analysis and active stabilization of the vsc-hvdc system,” in *IECON 2017-43rd Annual Conference of the IEEE Industrial Electronics Society*. IEEE, 2017, pp. 4891–4896.
- [15] L. Harnefors, M. Bongiorno, and S. Lundberg, “Input-admittance calculation and shaping for controlled voltage-source converters,” *IEEE transactions on industrial electronics*, vol. 54, no. 6, pp. 3323–3334, 2007.
- [16] M. Beza and M. Bongiorno, “Identification of resonance interactions in offshore-wind farms connected to the main grid by mmc-based hvdc system,” *International Journal of Electrical Power & Energy Systems*, vol. 111, pp. 101–113, 2019.
- [17] J. C. Willems, “Dissipative dynamical systems part i: General theory,” *Archive for rational mechanics and analysis*, vol. 45, no. 5, pp. 321–351, 1972.
- [18] X. Zhang, X. Ruan, and K. T. Chi, “Impedance-based local stability criterion for dc distributed power systems,” *IEEE Transactions on Circuits and Systems I: Regular Papers*, vol. 62, no. 3, pp. 916–925, 2015.
- [19] D. Furkan and M. Mehmet Emin, “Critical factors that affecting efficiency of solar cells,” *smart grid and renewable energy*, vol. 2010, 2010.

# A

## Appendix 1

### A.1 Capacitance Calculation of Capacitor Bank

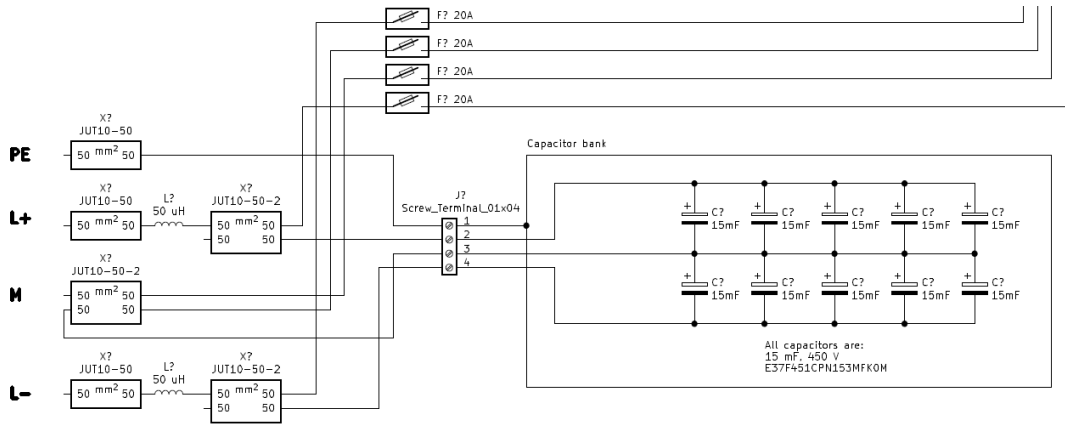


**Figure A.1:** Capacitor bank schematic of the real system.

Figure A.1 is the schematic of the real capacitor bank in the system, where each capacitor is 15 mF with a voltage rating of 450 V and a total VSC power rating of 3x28 kW. Converting this to our system with only one 28 kW VSC and 380 V between L+/L- and M, the new capacitance is calculated as

$$C_{new} = C_{old} \frac{S_{b_{new}}}{S_{b_{old}}} \frac{V_{b_{old}}^2}{V_{b_{new}}^2} \quad (\text{A.1})$$

$$C_{new} = 15 \cdot 10^{-3} \frac{28 \cdot 10^3}{3 \cdot 28 \cdot 10^3} \frac{450^2}{380^2} = 7.011 \cdot 10^{-3} F \quad (\text{A.2})$$